

Article

# Dynamic Analysis of Three-Rotor System with Hollow Shaft under Clutch Misalignment

Guofang Nan <sup>\*</sup>, Haoyu Wang and Dengliang Yu

School of Energy and Power Engineering, University of Shanghai for Science and Technology, Shanghai 200093, China; 232230038@st.usst.edu.cn (H.W.); 232230036@st.usst.edu.cn (D.Y.)

\* Correspondence: ngf@usst.edu.cn

**Abstract:** Rotor system of aviation engines is often made of multiple rotors connected by the clutch. Due to manufacturing and assembly errors, there is a clutch misalignment, including the parallel misalignment and the angle misalignment. This misalignment produces additional torque in the operation of the system, leading to an abnormal increase in its oscillation, which causes the rubbing between the stator and the rotor. The rub-collision poses great harm to the safety and stability of the aero-engine. The analytical model of the rotor system with misalignment and rubbing faults is established, and the influence of the rotational speed, the misalignment, and the rubbing on the nonlinear characteristics of the rotor is investigated. Considering the nonlinear Hertz contact force and bearing gap, the model of the inter-shaft bearing is built; the parallel and angle misalignments of clutch are taken into account to analyze the characteristic frequency of the faults. For raising the thrust-to-weight ratio of aviation engines, the hollow shaft is often adopted, and the effect of the wall thickness for the shaft on the nonlinear vibration of the system is also investigated. It is innovative to study the transfer mechanism from wall thickness to the nonlinear vibrational responses of the overall structure. The result indicates that, with the increase in the wall thickness of the shaft, the second critical rotating speed increases, while the first critical rotating speed is almost unchanged. The characteristic frequencies for the three-rotor system with coupling faults are obtained. Despite intuition, the parallel misalignment can inhibit rub-collision vibration to a certain extent. The research has important reference values for the fault recognition and structural optimization of the three-rotor system.



**Citation:** Nan, G.; Wang, H.; Yu, D. Dynamic Analysis of Three-Rotor System with Hollow Shaft under Clutch Misalignment. *Aerospace* **2024**, *11*, 319. <https://doi.org/10.3390/aerospace11040319>

Academic Editor: Ephraim Suhir

Received: 10 March 2024

Revised: 14 April 2024

Accepted: 16 April 2024

Published: 19 April 2024



**Copyright:** © 2024 by the authors. Licensee MDPI, Basel, Switzerland. This article is an open access article distributed under the terms and conditions of the Creative Commons Attribution (CC BY) license (<https://creativecommons.org/licenses/by/4.0/>).

**Keywords:** three-rotor system; rub-collision; misalignment; hollow shaft; dynamic behavior

## 1. Introduction

Compared with the traditional single-rotor system, the multi-rotor structure has a better performance; thus, it is widely used in aviation engines, gas turbines, and other transportation and energy production fields. The rotor structures are often connected by the clutch. Due to manufacturing or installation errors, there is parallel misalignment or angle misalignment of the rotors at the clutch, and the type of misalignment leads to an abnormal increase in rotor vibration. When the vibration is greater than the stationary clearance, the rotor and the stator collide. Rub-collision causes cracks or even damage to rotor components, such as the blades, the casings, and the clapboards. Hence, it is of momentous academic worth and application value for structural design and fault identification to investigate the dynamic characteristics of the rotor system with coupling faults.

Recently, the identification and diagnosis of the rubbing-impact fault for the rotor system have attracted the attention of scholars. Fu et al. [1] researched the uncertain dynamic behavior of the dual-rotor system with rubbing faults, and a surrogate model combined with the efficient polar angle interpolation (PAI) was developed to predict the response range affected by uncertainty. A dynamical model of the rotor system under the consideration of rub-collision and squeeze oil film forces was built by the FEM [2].

The influences of the rubbing-impact rigidity, the oil film gap, and the bearing clearance on the vibrational responses of the system were studied in detail. The research result indicated that the oil film gap has the largest influence on the dynamical characteristics of the system. Zhao et al. [3] developed the rubbing-impact dynamical model of the bearing system and studied the influence of the operating variables on the behavior of the falling rotor system, and they found that the power amplifier failure led to the maximum degree of rotor dropping collision achieved by experiments. Song et al. [4] studied the nonlinear dynamic behaviors of an aviation engine drum with the rubbing-impact faults of the rotor and stator blades, and the theoretical research results were confirmed by experiments. A new method for identifying the rubbing faults of the rotor system by energy characteristics was proposed by Zhang et al. [5]. Xu et al. [6] studied the vibrational characteristics of the spindle-bearing-housing-belt system with rub-collision by the means of the theoretical modeling method and FEA, and the results showed that the dynamic parameters of the belt have little effect on the vibrational response of the system. Hou et al. [7] revealed the law of frequency modulation through the simulation and experimentation of the blade-casing friction and developed an empirical formula for judging the type of rub-collision fault based on the law. Jin et al. [8] revealed the nonlinear vibration characteristics of a dual-rotor-bearing-coupled misalignment system with local blade rub-collision fault through numerical analysis and experimental validation. Li et al. [9] proposed an approach to represent the rub-collision fault by detecting the dynamic loads on the rotor and the stator.

Many scholars have also conducted several studies on the misalignment of the rotor system. Wang et al. [10] constructed an analytical model of the dual-rotor structure to study the vibrational characteristics of the rotor system with the imbalance and misalignment by the means of the experiments and numerical calculations. Huang et al. [11] presented a novel method to calculate the rigidity of the spline clutch, and the correctness of the method was validated by the means of the FEA. Tiwari et al. [12] developed the algorithm for identifying the faults of the magnetically levitated flexible rotor system, including the imbalance, the misalignment, and so on. Prasad V et al. [13] investigated the rotor system with the imbalance and misalignment by applying the support vector machine and conducted the related experiment to validate the accuracy of the method. Zhang et al. [14] constructed the universal model of the spline joint by considering the stationary and dynamical misalignments and explored the effect of the misalignment on the vibrational responses of the system. Zhao et al. [15] researched the effect of the misalignment of rolling bearing rings on the vibrational responses of the rotor systems. Through the analysis of the contact model between the rollers and the rings, it is proven that the back loading can increase the contact stability of the system. Tang et al. [16] investigated the influence of operating variables and fault factors on the system via theory and experiment, and the results showed that the angle misalignment has almost no influence on the dynamic responses, and the effect of the rubbing is remarkable. Xu et al. [17] presented a novel approach combining the Newton–Raphson and the Newmark- $\beta$  methods to study the vibrational responses of the rolling element system with the misalignment fault. Wang et al. [18] investigated the vibrational responses of the angle misalignment and the cage break faults by simulation analysis and experiments. The results indicate that the cage fracture leads to the increase in the amplitude of the system. Wu et al. [19] researched the random base motions of the rotor system with a misalignment fault in DMU, and the research shows that the nonlinear response of the DSM to the deterministic base motion is faster than the vibration of the rotor. Tuckmantel et al. [20] researched the vibration signal of the multi-span rotor structure with clutch under angle misalignment. Lees [21] studied the parallel misalignment in rigid rotors connected by bolts, and the expressions of amplitude and the phase of the nonlinear vibration were developed.

The complex coupling faults in the rotor system have been studied by many researchers. Fu et al. [22] investigated the nonlinear vibration of the hydraulic turbine with the imbalance, the misalignment, and the rubbing faults. Lu et al. [23] analyzed the dynamic behavior of the dual-rotor system with the misalignment, the rubbing, and the coupling

fault, respectively. Jin et al. [24] developed an approach that was applied for identifying the position of the cracks of the hollow rotor structure by CNN-C. Han et al. [25] presented a nonlinear joint element to study the dynamical responses of the bolt-connected rotor structure with the skewness of disk. Chen et al. [26] proposed a novel HB-AFT approach to investigate the vibrational responses of the rotor-bearing-casing system, and the approach is more efficient than the traditional method. Fan et al. [27] analyzed the bifurcation characteristic in the rub vibration of a piecewise linear stator–rotor system. Lu et al. [28] adopted the POD approach to reduce dimension of the rotor structure and conducted the corresponding experiments to validate the correctness of the proposed method. Li et al. [29] developed a fault diagnosis model frame of the rotor-bearing system. The model based on deep convolutional generative adversarial networks (TF-DLGANs) shows an excellent fault diagnosis performance. Xiang et al. [30] proposed a new transfer unsupervised learning approach for the fault diagnosis of the rotor in the experiment.

Researchers have conducted a significant amount of research on the rotor systems with rubbing–misalignment coupling faults. However, most of the research objects are single-rotor or dual-rotor system, and little research has been conducted on three rotors with coupling faults. The analytical model of the three-rotor system with angle and parallel misalignment faults is built in this paper; the effects of the rotating speed, the misalignment parameters of the clutch, the rubbing parameters, and the wall thickness of the hollow shaft on the dynamics of the system are studied. It is novel to conduct research on the transfer mechanism from the wall thickness to the dynamic responses of the three-rotor system. Compared with the traditional study of the rotor system with faults, the research object and research content of this paper have certain novelty, and the studies have crucial academic worth and application worth for fault recognition and structural optimization of the three-rotor system.

## 2. Modeling of the Three-Rotor-Bearing System

### 2.1. Physical Model of Three-Rotor-Bearing System

The rotor structure in an aviation engine is composed of multiple rotors in which the dual-rotor system is often connected by the inter-shaft bearings. Figure 1 is a schematic diagram of the physical model of the three-rotor system. Both ends of the low-pressure (LP) hollow rotor system are connected to the stator by the bearing 1 and bearing 2, and the clutch is supported by the bearing 3 and 4; one end of the high-pressure (HP) rotor is connected to the stator at the bearing 5, and the other end is connected to the LP turbine by the bearing 6, which is called the inter-shaft bearing. The position relationship and size of each structure of the rotor system are presented in Figure 1.

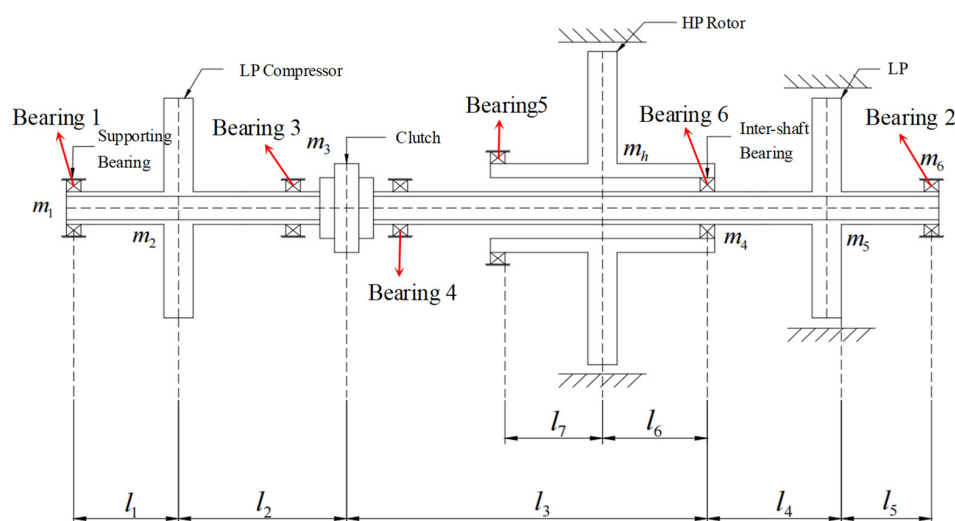


Figure 1. Physical model of the three-rotor structures.

This study focuses on the overall vibration characteristics of the three-rotor structures. For convenient calculation and analysis, the HP shaft is regarded as the rigid shaft in modeling, the torsional vibration and axial vibration are ignored, and the effect of temperature is also neglected. The lumped mass of the LP rotor at the bearing 1 is  $m_1$ ; the lumped mass of the impeller for the LP compressor is  $m_2$ ; the sum of the clutch mass and the rotor mass at bearing 3 and bearing 4 is  $m_3$ ; the lumped mass of the LP rotor at bearing 6 is  $m_4$ ; the concentrated mass of the disk for the LP turbine is  $m_5$ ; the lumped mass of the LP rotor at the bearing 2 is  $m_6$ ; the centralized mass of the disk for the HP rotor is  $m_h$ . The support stiffness and damping of the bearing 1, bearing 2, bearing 3, bearing 4, and bearing 5 are  $k_1, c_1, k_2, c_2, k_3, c_3, k_4, c_4, k_5, c_5$ , respectively. The displacements of each concentrated mass are  $x_1, y_1, x_2, y_2, x_3, y_3, x_4, y_4, x_5, y_5, x_6, y_6, x_h, y_h$ , respectively. The rotating degrees of the HP rotor around the  $x$  axis and the  $y$  axis are  $\theta_x$  and  $\theta_y$ , respectively. The eccentricities of the HP rotor, the LP compressor, and the LP turbine are  $e_h, e_1, e_2$ , respectively. The flexible modulus for the LP shaft is  $E$ , and the moment of inertia for the cross-section is  $I$ . The polar moment of inertia for the LP disk is  $J_p$ , and the diameter moment of inertia for the disk is  $J_d$ . The material damping of the shaft segment between the lumped mass  $i$  and  $j$  is  $c_{ij}$ . The rotational speed ratio of the HP rotor and the LP rotor is  $\lambda$ .

In order to study the dynamics of the multi-rotor structure with misalignment and rub-collision faults, an accurate analytical model composed of the rub-collision, the rolling element bearing, and the misalignment of clutch should be established. The detailed modeling procedure is as follows.

## 2.2. Contact Model of the Rotor and the Stator

The rub-collision of the rotor and the stator for the three-rotor system with discs may occur in the HP rotor or the LP turbine, or in both simultaneously. As the radial displacements of the rotor are larger than the gap, the collision-rub occurs between the rotor and the stator, and the collision-rub model is shown in Figure 2; two instantaneous forces appear at the contact point, one is the normal impact force that is described by the linear spring model; the other is the tangential friction force that is described by the Coulomb friction model. Both of these forces exhibit non-smooth properties and are dependent on the vibrational amplitudes of the rotor, as shown in Equation (1); as the radial displacements of the rotor are less than the gap, the collision-rub does not exist.

$$\begin{cases} P_n(x, y) = k_p(\sqrt{x^2 + y^2} - \delta) \\ P_\tau(x, y) = fP_n \end{cases}, \text{ if } \sqrt{x^2 + y^2} - \delta \geq 0 \quad (1)$$

where  $k_p$  represents the impact stiffness;  $f$  represents the coefficient of friction between the rotor and the stator; and  $\delta$  denotes the stationary clearance between the rotor and the stator;  $x$  and  $y$  denote the lateral displacements of the rotor. By projecting  $P_n$  and  $P_\tau$  onto the  $x$  axis and the  $y$  axis, the force components can be expressed as Equation (2).

$$\begin{cases} P_x = k_p(x - fy)(1 - \frac{\delta}{\sqrt{x^2 + y^2}}) \\ P_y = k_p(fx + y)(1 - \frac{\delta}{\sqrt{x^2 + y^2}}) \end{cases}, \text{ if } \sqrt{x^2 + y^2} - \delta \geq 0 \quad (2)$$

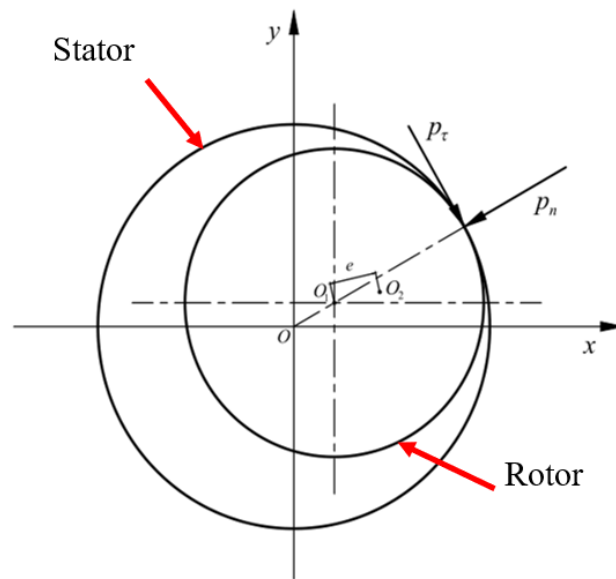


**Figure 2.** Contact model of the rotor and the stator.

2.3. Modeling of Inter-Shaft Bearing

The rolling bearings are generally applied in an aviation engine, and the intermediary bearing, which is one type of rolling bearing, is used to connect the HP and LP rotors. The type of bearing has an important effect on the dynamics of the rotor system because of the two connecting rotors. Therefore, it is indispensable to make a fine model for the inter-shaft bearing, and the basic assumptions are as follows.

- (a) Ignore the friction and the relative sliding between the rolling element and the inner raceway and the outer raceway.
- (b) The rolling element and the inner and outer rings only have a radial flexible force that satisfies the Hertz contact theory.
- (c) The rolling elements are evenly arranged and spaced equally between the inner and outer rings.
- (d) The inner ring and outer ring of the bearing are rigidly connected to the shafts, with no relative sliding.

The schematic diagram of the physical model for the inter-shaft bearing is presented in Figure 3. The line velocities of the contact point between the rolling elements and the inner ring and the outer ring are  $v_r$  and  $v_R$ , respectively. The rotating velocities of the inner and outer raceways are  $\omega_r$  and  $\omega_R$ , respectively. If the linear and angular velocities for the cage are  $v_{cage}$  and  $\omega_{cage}$ , respectively, the expressions of  $v_r$ ,  $v_R$ , and  $v_{cage}$  are as follows:

$$\begin{cases} v_r = \omega_r \times r \\ v_R = \omega_R \times R \end{cases} \tag{3}$$

$$v_{cage} = \frac{1}{2}(v_r + v_R) \tag{4}$$

Because the inner ring and the outer ring of the bearing are rigidly connected with the shafts, and there is no relative rotation between the rings and the shafts, and the angular velocity of the cage is maintained as follows:

$$\omega_{cage} = \frac{v_r \times r + v_R \times R}{r + R} \tag{5}$$

The continuous periodic change in the bearing stiffness and the unbalanced force of the bearing lead to the varying compliance (VC) vibration of the rolling bearing. The vibrational frequency caused by the unbalanced force is the rotation frequency of the rotor.

Assuming that the number of rolling elements is  $N_b$ , then, the passing frequency of rolling elements is as follows:

$$\omega_{vc} = N_b \times \omega_{cage} \tag{6}$$

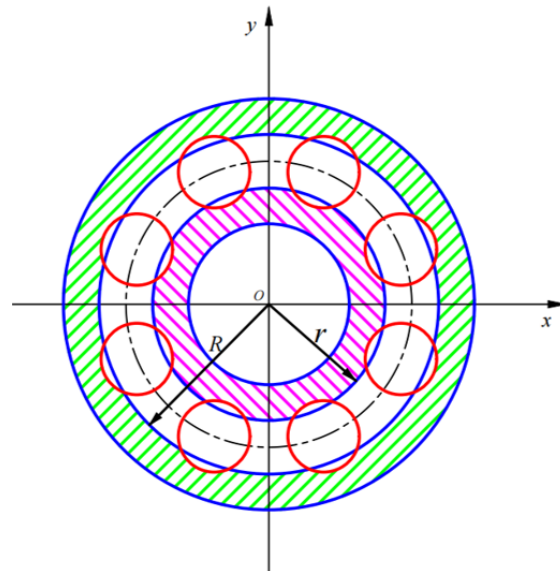


**Figure 3.** Physical model of rolling bearing.

The contact angle of the  $j$  rolling element is  $\theta_j$ , the normal contact deformation of the  $j$  rolling element is  $\delta_j$ , and the clearance of the intermediate bearing is  $\varepsilon$ ; then, the obtained equations are as follows:

$$\theta_j = \omega_{cage} \times t + (j - 1) \frac{2\pi}{N_b} \tag{7}$$

$$\delta_j = x \cdot \cos \theta_j + y \cdot \sin \theta_j - \varepsilon \tag{8}$$

Based on the Hertz flexible contact theory, the contact force between the  $j$  rolling element and the raceway is as follows:

$$F_j = K_b \cdot \delta_j^{1.5} \times H(\delta_j) \tag{9}$$

where  $K_b$  is the contact stiffness of the rolling bearing,  $H$  is the Heaviside step function. After the force of each rolling element is concentrated on the centroid of the rolling bearing, the radial bearing force of the rolling bearing is as follows:

$$\begin{cases} F_x = \sum_{j=1}^{N_b} F_{jx} = \sum_{j=1}^{N_b} K_b (x \cos \theta_j + y \sin \theta_j - \varepsilon)^{1.5} \times H(x \cos \theta_j + y \sin \theta_j - \varepsilon) \cos \theta_j \\ F_y = \sum_{j=1}^{N_b} F_{jy} = \sum_{j=1}^{N_b} K_b (x \cos \theta_j + y \sin \theta_j - \varepsilon)^{1.5} \times H(x \cos \theta_j + y \sin \theta_j - \varepsilon) \sin \theta_j \end{cases} \tag{10}$$

#### 2.4. Modeling of Clutch Misalignment

The parallel misalignment and the angle misalignment of the clutch are considered in this modeling. The schematic diagrams of the rotor misalignment are presented in Figure 4 where  $\omega_2$  is the rotational speed of the LP rotor,  $\Delta e$  represents the parallel misalignment, and  $\alpha$  denotes the angular misalignment.

The rotor system is driven by airflow that makes the turbine disk rotate. Because the supports at both ends of the rotor have different centers, there is an angle between the shaft and the torque of the driving force, and the angle brings additional moment of flexure to the system. The analysis of the misalignment torque is presented in Figure 5. By decomposing  $T$  into the direction of the shaft and the direction vertical to the shaft,

respectively,  $T_\alpha$  and  $T_s$  are obtained. The moment caused by the airflow exciting force is leftward, the angle of the misalignment is  $\alpha$ , and the intersection angle between the  $y$  axis and  $T_s$  is  $\beta$ . By decomposing  $T_s$  in the  $x$ -axis direction and the  $y$ -axis direction, respectively,  $T_x$  and  $T_y$  are acquired.

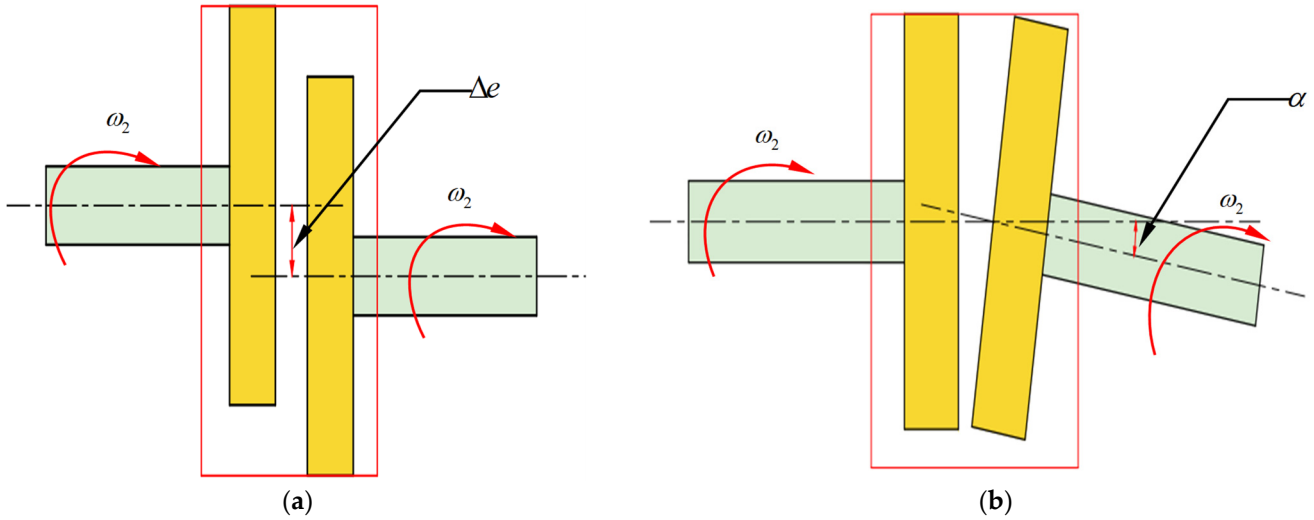


**Figure 4.** Schematic diagram of the misalignment of the LP rotor system: (a) parallel misalignment and (b) angular misalignment.

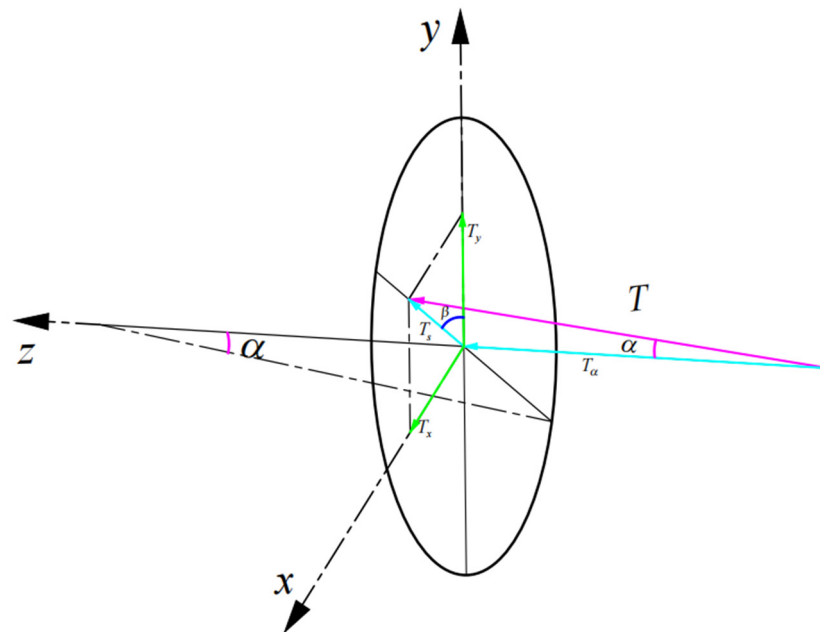


**Figure 5.** Misalignment torque analysis.

Based on the geometrical relationships, the equations that can be obtained are as follows:

$$T_\alpha = T \cos \alpha \tag{11}$$

$$T_s = T \sin \alpha \tag{12}$$

$$T_x = T_s \cos \beta = T \sin \alpha \cos \beta \tag{13}$$

$$T_y = T_s \sin \beta = T \sin \alpha \sin \beta \tag{14}$$

Assuming that the misalignment displacements of the bearings at both ends of the rotor system are  $\Delta x$  and  $\Delta y$ , respectively, during the actual operation of the rotor system, then, the obtained equations are as follows:

$$\alpha = \arctan \frac{\sqrt{\Delta x^2 + \Delta y^2}}{l} \quad (15)$$

$$\beta = \arctan \frac{\Delta y}{\Delta x} \quad (16)$$

Since the lateral displacement of the rotor at the bearing is far less than the length of the bearing,  $\alpha$  and  $\beta$  are treated as constants. Based on the Euler's equation,  $T_x$ ,  $T_y$ , and  $T_z$  are expressed as follows:

$$\begin{cases} T_x = I_x \dot{\omega}_x + \omega_y \omega_z (T_y - T_z) \\ T_y = I_y \dot{\omega}_y + \omega_z \omega_x (T_z - T_x) \\ T_z = I_z \dot{\omega}_z + \omega_x \omega_y (T_x - T_y) \end{cases} \quad (17)$$

where  $\omega_i$  is the angular velocity for the rotor;  $I_i$  is the main moment of inertia from the rotor to the shaft,  $I = x, y, z$ .

Because the rotor rotates around the  $z$  axis,  $\omega_x = \omega_y = \dot{\omega}_x = \dot{\omega}_y = 0$ , the Euler's equation for rotating around the fixed point can be simplified as follows:

$$T_z = T \cos \alpha = I_z \varepsilon_z \quad (18)$$

where  $\varepsilon_z$  is the angular acceleration for the rotor.  $I_z$  can be expressed as follows:

$$I_z = \frac{\pi}{64} [D^4 - (D - 2 \times \Delta d)^4] \quad (19)$$

where  $D$  denotes the outer diameter of the LP shaft, and the  $\Delta d$  is the wall thickness of the LP shaft. The relationship of the angular velocity and the misalignment angle is written as follows:

$$\omega / \omega_d = M / (1 + N \cos 2\theta_d) \quad (20)$$

where  $\omega$  is the rotational angular velocity of the rotor,  $\omega_d$  is the angular velocity of the turbine disk excited by the airflow, and  $\theta_d$  represents the angular displacement for the turbine disk. The rotating speed of the turbine disk and the rotor is approximately equal under a small-angle misalignment.  $M$  and  $N$  are coefficients related to the misalignment angle.

$$\begin{cases} M = 4 \cos \alpha / (3 + \cos 2\alpha) \\ N = (1 - \cos 2\alpha) / (3 + \cos 2\alpha) \end{cases} \quad (21)$$

Considering the differential of  $\beta$ , the angular acceleration can be expressed as follows:

$$\varepsilon_z = \frac{2MN \sin(2\omega t)}{[1 + N \cos(2\omega t)]^2} \omega^2 \quad (22)$$

By substituting Equation (21) into the Euler equation, torque  $T$  can be written as follows:

$$T = \frac{2I_z \omega^2 MN \sin(2\omega t)}{[1 + N \cos(2\omega t)]^2 \cos \alpha} \quad (23)$$

The misalignment torque is decomposed into each axis, and each component can be expressed as follows:

$$T_x = \frac{2I_z \omega^2 MN \sin(2\omega t)}{[1 + N \cos(2\omega t)]^2 \cos \alpha} \tan \alpha \sin \beta \quad (24)$$

$$T_y = \frac{2I_z \omega^2 MN \sin(2\omega t)}{[1 + N \cos(2\omega t)]^2 \cos \alpha} \tan \alpha \cos \beta \tag{25}$$

2.5. Equation of Motion for the Three-Rotor System

For studying the nonlinear dynamic characteristics of the misalignment–rubbing coupling of the three-rotor system, the equation of motion for the system should be developed first. The kinetic energy of the high-pressure rotor can be expressed as follows:

$$E_k = \frac{1}{2} m_h (\dot{x}_h^2 + \dot{y}_h^2) + \frac{1}{2} J_d (\dot{\theta}_h^2 + \dot{\theta}_x^2) + \frac{1}{2} J_p \omega_1^2 - J_p \omega_1 \dot{\theta}_x \dot{\theta}_y \tag{26}$$

The potential energy of the high-pressure rotor can be written as follows:

$$E_p = \frac{1}{2} k_5 (x_{h1}^2 + y_{h1}^2) \tag{27}$$

where  $x_{h1}$  and  $y_{h1}$  are the lateral displacements at support 5,

$$\begin{cases} x_{h1} = x_h - \theta_y l_7 \\ y_{h1} = y_h - \theta_x l_7 \end{cases} \tag{28}$$

and the dissipation energy of high-pressure rotor is given by the following:

$$E_d = \frac{1}{2} c_5 (\dot{x}_{h1}^2 + \dot{y}_{h1}^2) \tag{29}$$

The external forces of the HP rotor include the imbalance, the rubbing force, the gravity, and the support force of the intermediate bearing. Applying the Lagrange equation, the equations of motion for the HP rotor are established as follows:

$$\begin{cases} m_h \ddot{x}_h + k_5(x_h - \theta_y l_6) + c_5(\dot{x}_h - \dot{\theta}_y l_6) = F_x + m_h e_h \omega_1^2 \cos(\omega_1 t) + P_{x1} \\ J_d \ddot{\theta}_y - \frac{1}{2} J_p \omega_1 \dot{\theta}_x - k_5 l_6 (x_h - \theta_y l_6) - c_5 l_6 (\dot{x}_h - \dot{\theta}_y l_6) = F_x l_6 + T_x \\ m_h \ddot{y}_h + k_5(y_h + \theta_x l_6) + c_5(\dot{y}_h + \dot{\theta}_x l_6) = F_y + m_h e_h \omega_1^2 \sin(\omega_1 t) + P_{y1} + m_h g \\ J_d \ddot{\theta}_x + \frac{1}{2} J_p \omega_1 \dot{\theta}_y + k_5 l_6 (y_h + \theta_x l_6) + c_5 l_4 (\dot{y}_h + \dot{\theta}_x l_6) = -F_y l_7 + T_y \end{cases} \tag{30}$$

where  $P_{x1}$  and  $P_{y1}$  denote the components of the rubbing force of the HP disc in the  $x$  direction and the  $y$  direction, respectively.

Based on Newton’s second law, the equation of motion for the LP rotor is developed and is as follows:

$$\begin{cases} m_1 \ddot{x}_1 + k_1 x_1 + c_1 \dot{x}_1 + k_{12}(x_1 - x_2) + c_{12}(\dot{x}_1 - \dot{x}_2) = 0 \\ m_1 \ddot{y}_1 + k_1 y_1 + c_1 \dot{y}_1 + k_{12}(y_1 - y_2) + c_{12}(\dot{y}_1 - \dot{y}_2) = -m_1 g \\ m_2 \ddot{x}_2 + k_{12}(x_2 - x_1) + c_{12}(\dot{x}_2 - \dot{x}_1) + k_{23}(x_2 - x_3) + c_{23}(\dot{x}_2 - \dot{x}_3) = m_2 e_1 \omega_2^2 \cos(\omega_2 t) \\ m_2 \ddot{y}_2 + k_{12}(y_2 - y_1) + c_{12}(\dot{y}_2 - \dot{y}_1) + k_{23}(y_2 - y_3) + c_{23}(\dot{y}_2 - \dot{y}_3) = -m_2 g + m_2 e_1 \omega_2^2 \sin(\omega_2 t) \\ m_3 \ddot{x}_3 + k_3 x_3 + c_3 \dot{x}_3 + k_{23}(x_3 - x_2) + c_{23}(\dot{x}_3 - \dot{x}_2) + k_{34}(x_3 - x_4) + c_{34}(\dot{x}_3 - \dot{x}_4) = m_3 \Delta e (2\omega_2)^2 \cos(2\omega_2 t) \\ m_3 \ddot{y}_3 + k_3 y_3 + c_3 \dot{y}_3 + k_{23}(y_3 - y_2) + c_{23}(\dot{y}_3 - \dot{y}_2) + k_{34}(y_3 - y_4) + c_{34}(\dot{y}_3 - \dot{y}_4) = -m_3 g + m_3 \Delta e (2\omega_2)^2 \sin(2\omega_2 t) \\ m_4 \ddot{x}_4 + k_{34}(x_4 - x_3) + c_{34}(\dot{x}_4 - \dot{x}_3) + k_{45}(x_4 - x_5) + c_{45}(\dot{x}_4 - \dot{x}_5) = -F_x \\ m_4 \ddot{y}_4 + k_{34}(y_4 - y_3) + c_{34}(\dot{y}_4 - \dot{y}_3) + k_{45}(y_4 - y_5) + c_{45}(\dot{y}_4 - \dot{y}_5) = -F_y - m_4 g \\ m_5 \ddot{x}_5 + k_{45}(x_5 - x_4) + c_{45}(\dot{x}_5 - \dot{x}_4) + k_{56}(x_5 - x_6) + c_{56}(\dot{x}_5 - \dot{x}_6) = P_{x2} + m_5 e_2 \omega_2^2 \cos(\omega_2 t) \\ m_5 \ddot{y}_5 + k_{45}(y_5 - y_4) + c_{45}(\dot{y}_5 - \dot{y}_4) + k_{56}(y_5 - y_6) + c_{56}(\dot{y}_5 - \dot{y}_6) = P_{y2} - m_5 g + m_5 e_2 \omega_2^2 \sin(\omega_2 t) \\ m_6 \ddot{x}_6 + k_2 x_6 + c_2 \dot{x}_6 + k_{56}(x_6 - x_5) + c_{56}(\dot{x}_6 - \dot{x}_5) = 0 \\ m_6 \ddot{y}_6 + k_2 y_6 + c_2 \dot{y}_6 + k_{56}(y_6 - y_5) + c_{56}(\dot{y}_6 - \dot{y}_5) = -m_6 g \end{cases} \tag{31}$$

where  $k_{ij}$  is the bending stiffness for the flexible shaft segment between the concentrated mass  $I$  and the concentrated mass  $j$ .

### 3. Analysis of Fault Features

The fault features of each rotor in the system are analyzed for fault diagnosis in this section, t. The main variables used in the calculation example are shown from Table 1, and the Runge–Kutta approach is applied to obtain the solution of Equation (31), and the initial transient data are abandoned, and the steady state data is kept for analysis. In order to investigate the fault characteristic for the multi-rotor system, with  $\Delta d = 4 \times 10^{-3}$  m, the waterfall diagrams of each rotor under no fault ( $\Delta e = 0, \alpha = 0, \delta_i > \forall \sqrt{x_i^2 + y_i^2}, \mu_i = 0$ ), only misalignment ( $\Delta e = 1 \times 10^{-5}, \alpha = 5, \delta_i > \forall \sqrt{x_i^2 + y_i^2}, \mu_i = 0$ ), only rubbing ( $\Delta e = 0, \alpha = 0, \delta_i = 5 \times 10^{-5}, \mu_i = 0.1$ ), coupling faults of misalignment, and rubbing ( $\Delta e = 1 \times 10^{-5}, \alpha = 5, \delta_i = 5 \times 10^{-5}, \mu_i = 0.1$ ) are drawn.

**Table 1.** Specific parameters of the multi-rotor system.

Parameters	Values	Parameters	Values
Lumped mass $m_1$ (kg)	1.5	Length of $l_1$ (m)	0.3
Lumped mass $m_2$ (kg)	6	Length of $l_2$ (m)	0.3
Lumped mass $m_3$ (kg)	10	Length of $l_3$ (m)	0.8
Lumped mass $m_4$ (kg)	2	Length of $l_4$ (m)	0.2
Lumped mass $m_5$ (kg)	6	Length of $l_5$ (m)	0.2
Lumped mass $m_6$ (kg)	1.5	Length of $l_6$ (m)	0.3
Lumped mass $m_i$ (kg)	8	Length of $l_7$ (m)	0.3
Support stiffness $k_1$ of bearing 1 (N/m)	$3 \times 10^6$	Damping coefficient $c_{12}$ of flexible shaft segment (N·s/m)	800
Support stiffness $k_2$ of bearing 2 (N/m)	$3 \times 10^6$	Damping coefficient $c_{23}$ of flexible shaft segment (N·s/m)	800
Support stiffness $k_3$ of bearing 3 (N/m)	$3 \times 10^6$	Damping coefficient $c_{34}$ of flexible shaft segment (N·s/m)	800
Support stiffness $k_4$ of bearing 4 (N/m)	$3 \times 10^6$	Damping coefficient $c_{45}$ of flexible shaft segment (N·s/m)	800
Support stiffness $k_5$ of bearing 5 (N/m)	$3 \times 10^6$	Damping coefficient $c_{56}$ of flexible shaft segment (N·s/m)	800
Support damping coefficient $c_1$ of bearing 1 (N·s/m)	1200	Polar moment of inertia $J_p$ (kg·m <sup>2</sup> )	0.04
Support damping coefficient $c_2$ of bearing 2 (N·s/m)	1200	Diameter moment of inertia $J_d$ (kg·m <sup>2</sup> )	0.02
Support damping coefficient $c_3$ of bearing 3 (N·s/m)	1200	The flexible modulus $E$ of the shaft (kg·m <sup>2</sup> )	$2 \times 10^{11}$
Support damping coefficient $c_4$ of bearing 4 (N·s/m)	1200	Inner-ring radius $r$ (m)	$40.1 \times 10^{-3}$
Support damping coefficient $c_5$ of bearing 5 (N·s/m)	1200	Outer-ring radius $R$ (m)	$63.9 \times 10^{-3}$
Mass eccentricity $e_1$ of LP compressor disk (m)	$5 \times 10^{-5}$	Rolling element number $N_b$	8
Mass eccentricity $e_2$ of LP turbine disk (m)	$5 \times 10^{-5}$	Stiffness $K_b$ of inter-shaft bearing (N/m)	$13.34 \times 10^9$
Mass eccentricity $e_i$ of HP rotor disk (m)	$3 \times 10^{-5}$	Clearance $\varepsilon$ of inter-shaft bearing (m)	$5 \times 10^{-6}$
The rotational speed ratio $\lambda$ of HP and LP rotors	1.6	Outer diameter $D$ of the LP shaft (m)	$3.936 \times 10^{-2}$

#### 3.1. LP Compressor

The waterfall diagrams of the LP compressor without fault and with various faults are shown in Figure 6. Comparing with Figure 6a, the new double frequency ( $2\times$ ) of the rotor vibration occurs only under the misalignment fault in Figure 6b, and the amplitude of  $2\times$  frequency is significantly larger than that of  $1.6\times$  frequency, and the amplitude of  $1\times$  frequency is slightly increased (only 0.35%). It is inferred that the new  $2\times$  frequency may be the characteristic frequency of the rotor misalignment fault. As can be seen in Figure 6a,c, the misalignment fault does not produce a new frequency doubling ( $2\times$ ), but only increases the amplitude of the  $1\times$  frequency by 2.05%. As can be seen in Figure 6d, under the action of the two faults, the amplitude peak caused by the superposition of rubbing and misalignment increases by 2.18%.

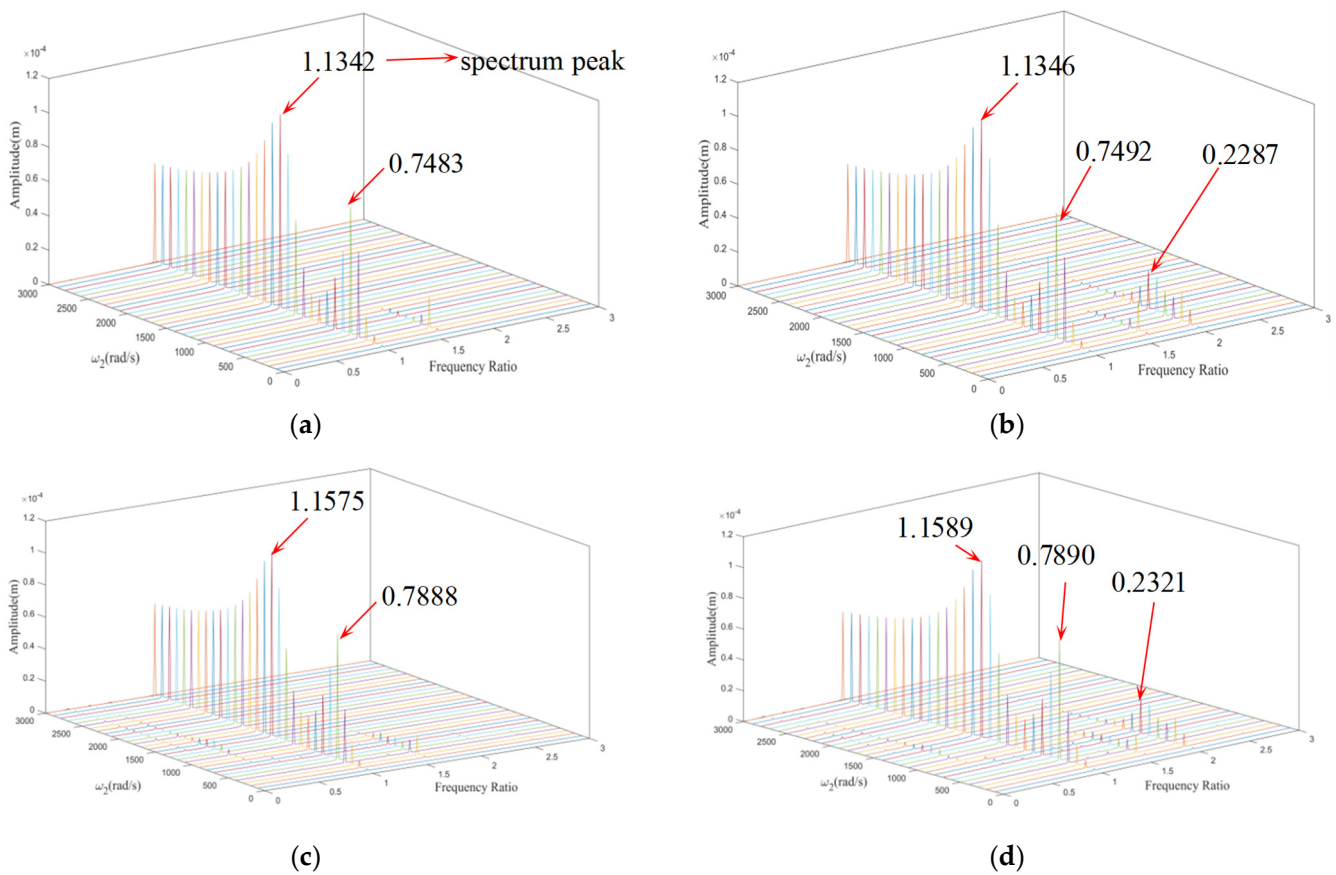


**Figure 6.** The waterfall diagrams of the LP compressor without fault and with various faults: (a) without fault; (b) only misalignment; (c) only rubbing; and (d) coupling fault of misalignment and rubbing.

### 3.2. LP Turbine

The waterfall diagrams of the LP turbine without fault and with various faults are presented in Figure 7. As can be shown from Figure 7a,b, the new  $2\times$  frequency component occurs only under the misalignment fault, and the amplitude of  $1\times$  frequency increases by 0.71%. Comparing Figures 7a and 7c, complex frequency components such as  $0.4\times$ ,  $0.2\times$ ,  $2.2\times$ , and  $2.6\times$  appear only under the rubbing fault, and the amplitude peak of the  $1\times$  frequency decreases by 48.80%. As can be shown from Figure 7d, the vibration of the LP turbine under coupling faults is more complex, but the overall amplitude-frequency characteristics are similar to those under only the rubbing fault, indicating that under coupling faults, the rubbing fault occupies the dominant position in influencing the rotor vibration. It can be inferred that the characteristic frequencies of the rubbing fault are  $0.4\times$ ,  $0.2\times$ ,  $2.2\times$ ,  $2.6\times$ , and other sub-harmonics, and rubbing has some inhibitory impact on the amplitude of the vibrational response.

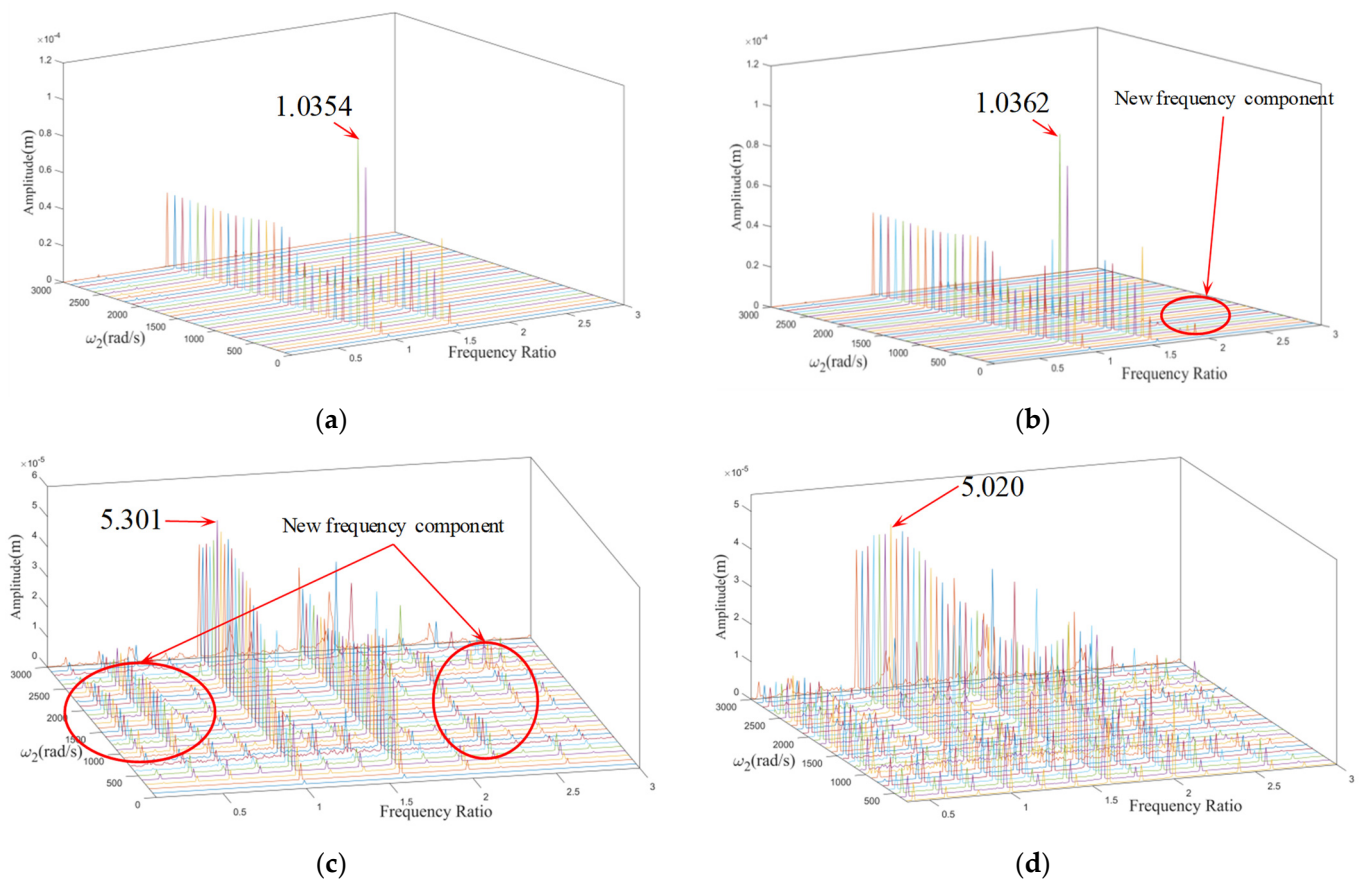


**Figure 7.** The waterfall diagrams of the LP turbine without fault and with various faults: (a) without fault; (b) only misalignment; (c) only rubbing; and (d) coupling fault of misalignment and rubbing.

### 3.3. HP Rotor

The waterfall diagrams of the HP rotor without fault and with various faults are presented in Figure 8, where the new minor  $2\times$  frequency occurs under only the misalignment fault. Comparing Figure 8a and Figure 8c, it can be seen that the relative relationship of each frequency component has changed significantly. The amplitude of the  $1\times$  frequency has decreased significantly, with a decrease of 84.70%, and the amplitude of  $1.6\times$  frequency has increased significantly, with a maximum increase of 158.55%. It can be observed from Figure 7d that the overall amplitude–frequency characteristics under coupling faults are similar to those under only rubbing, indicating that rubbing has a significant effect on the vibrational response of the rotor system under coupling faults. At the same time, the amplitude is slightly affected by misalignment, only with a decrease of 4.40%. For the HP rotor, the rubbing characteristic is that the  $1.6\times$  frequency component dominates the vibrations, and the misalignment has a somewhat inhibiting impact on the amplitudes of the vibrational response.

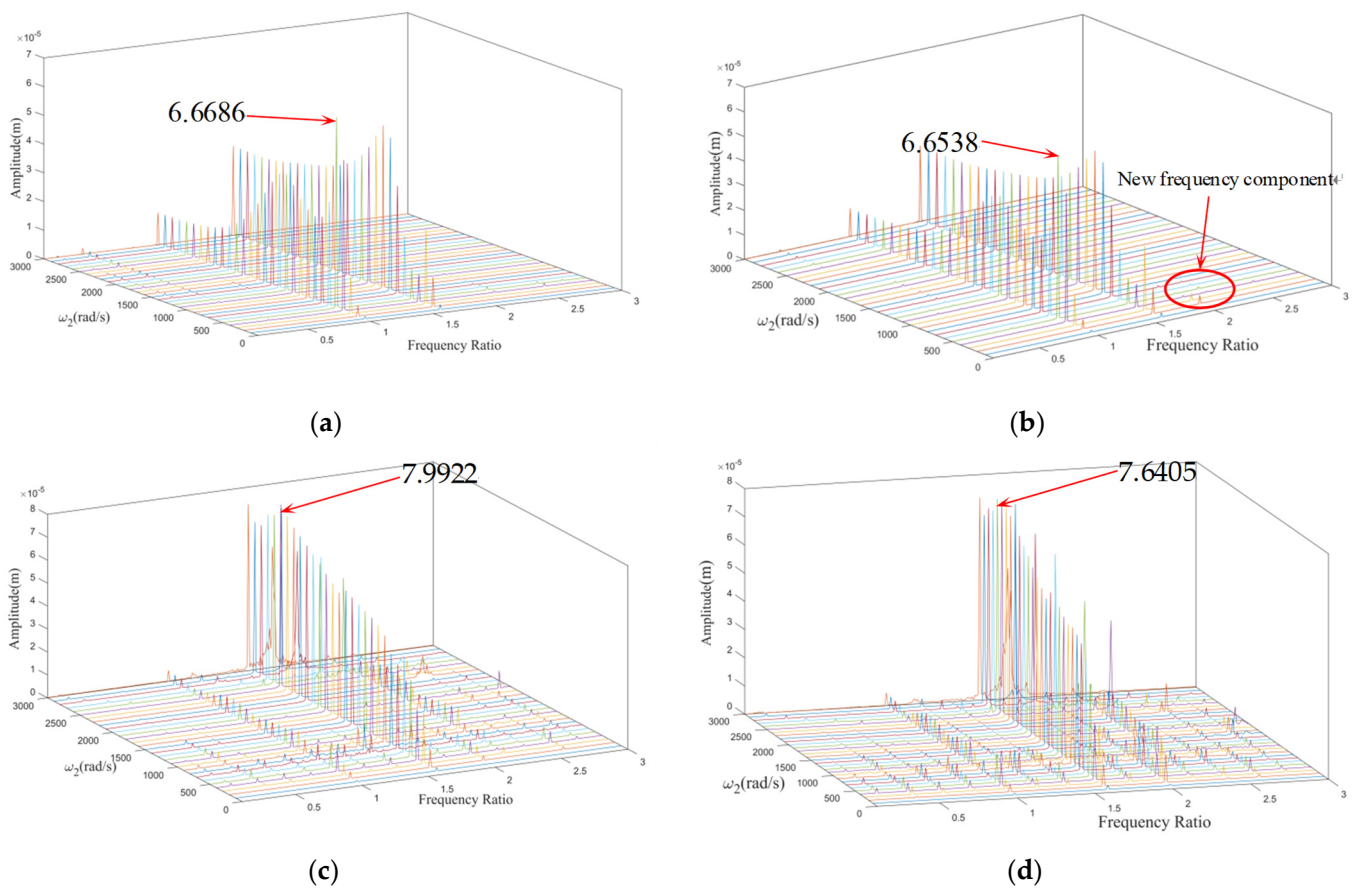


**Figure 8.** The waterfall diagrams of the HP rotor without fault and with various faults: (a) without fault; (b) only misalignment; (c) only rubbing; and (d) coupling fault of misalignment and rubbing.

### 3.4. Characteristic Frequency

In the three-rotor system, the LP compressor, the LP turbine, and the HP rotor all have  $2\times$  frequency when the system only has the misalignment fault; three rotors all have  $0.4\times$  frequency when the system only has the rub-collision fault; three rotors all have the superposition of the characteristic frequency when the system has coupling faults of misalignment and rub-collision. It can be inferred that, for this multi-rotor system, the characteristic frequency of the misalignment fault is  $2\times$ , and the characteristic frequency of rub-collision fault is  $0.4\times$ , which is often accompanied by  $0.6\times$ ,  $2.2\times$ , and other frequency components. The characteristic frequency of coupling faults mainly includes  $2\times$ ,  $0.4\times$ ,  $0.6\times$ , etc., and the frequency component is more complicated than that of a single fault. When the system has only the misalignment fault, the vibration amplitude of each rotor from large to small is for the LP compressor, the LP turbine, and the HP rotor. This difference is related to the distance of each rotor and the clutch, and the farther the distance is, the greater the vibration decay is. For the HP rotor, when there is a rub-collision fault, the  $1.6\times$  frequency component dominates the whole spectrum. This research is meaningful for the arrangement of sensors in fault diagnosis experiments.

## 4. Influencing Factors of Dynamic Characteristic for Multi-Rotor System

### 4.1. Influence of Rotational Speed

The most basic variable of the rotor system is the rotational speed. For studying the effect of the rotating speed on the nonlinear characteristics of the multi-rotor system, the speed range of  $100\sim 3000$  rad/s is chosen for the LP rotor, along with the rub-collision stiffness of  $k_{pi} = 4 \times 10^8$  N/m, the rub-collision gap of  $\delta = 5 \times 10^{-5}$  m, the misalignment angle  $\alpha = 5^\circ$ , and the clutch parallel misalignment  $\Delta e = 1 \times 10^{-5}$  m, and the bifurcation

diagram of the vibrational amplitude for the low-pressure turbine rotor with change in the speed is shown in Figure 9 where the system exhibits complex dynamical behaviors such as the periodic, multi-periodic, quasi-periodic, and chaotic motions with an increase in the rotating speed.

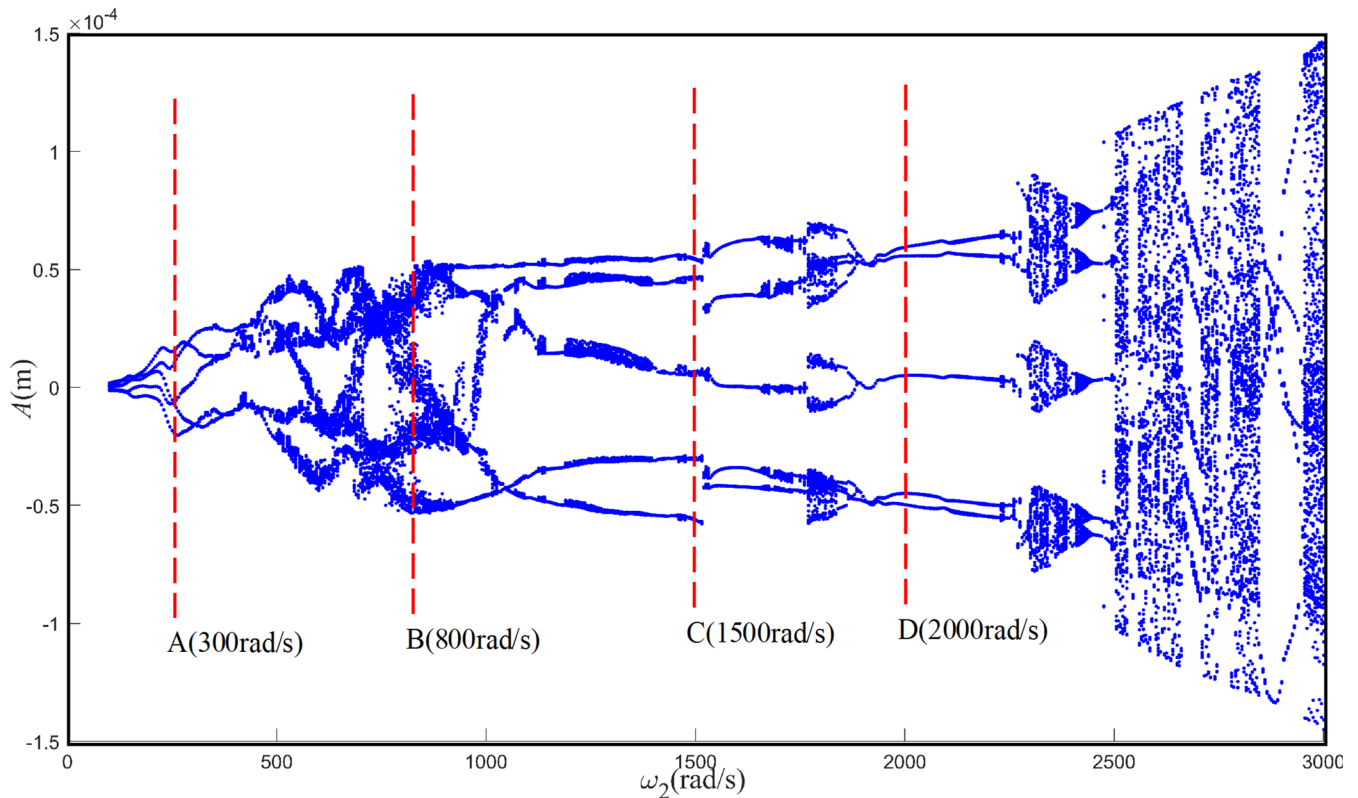


**Figure 9.** Rotational speed bifurcation diagram of low-pressure rotor.

The research object is the aero-engine rotor whose working speed has some gears, and the typical speeds are chosen at different gears. For studying the characteristics of each typical dynamic behavior, the typical rotating speeds of 300 rad/s, 800 rad/s, 1500 rad/s, and 2000 rad/s are selected, respectively, and the time history, the frequency spectrum, the Poincaré section, and the axis trajectory of the vibrational response of the low-pressure turbine are obtained, as shown in Figures 10–14. It can be shown from Figure 10 that the amplitude and frequency change with the increase in the rotational speed. As can be seen in Figure 11a, when the speed is 300 rad/s, the dominant frequency is  $1.6\times$ ; there are five independent points in the Poincaré diagram, indicating that the system is under the state of Period-5, as seen in Figure 11b; and the LP turbine rotor and the downside casing collide in the vertical direction, as seen in Figure 11c; the dominant frequency component is also  $1.6\times$ , as shown in Figure 12a; it can be shown from Figure 12b that, when the rotating speed is 800 rad/s, the spectrum becomes more complicated than that of 300 rad/s, and the Poincaré diagram presents the irregular scatter points; the axis trajectory becomes disordered, as seen in Figure 12c, indicating that the system is under a chaotic state. It can be seen in Figure 13 that, when the rotating speed is 1500 rad/s, the dominant frequency component is  $1\times$ , and the frequency components of the high-frequency part increase, and the amplitude of the  $4.4\times$  frequency is larger, as seen in Figure 13a; and five clusters of scattered points appear in the Poincaré diagram, as shown in Figure 13b, denoting that the system is under the quasi-periodic state at this time. It can be seen in Figure 14 that the system exhibits a periodic motion again as the rotation speed is 2000 rad/s.

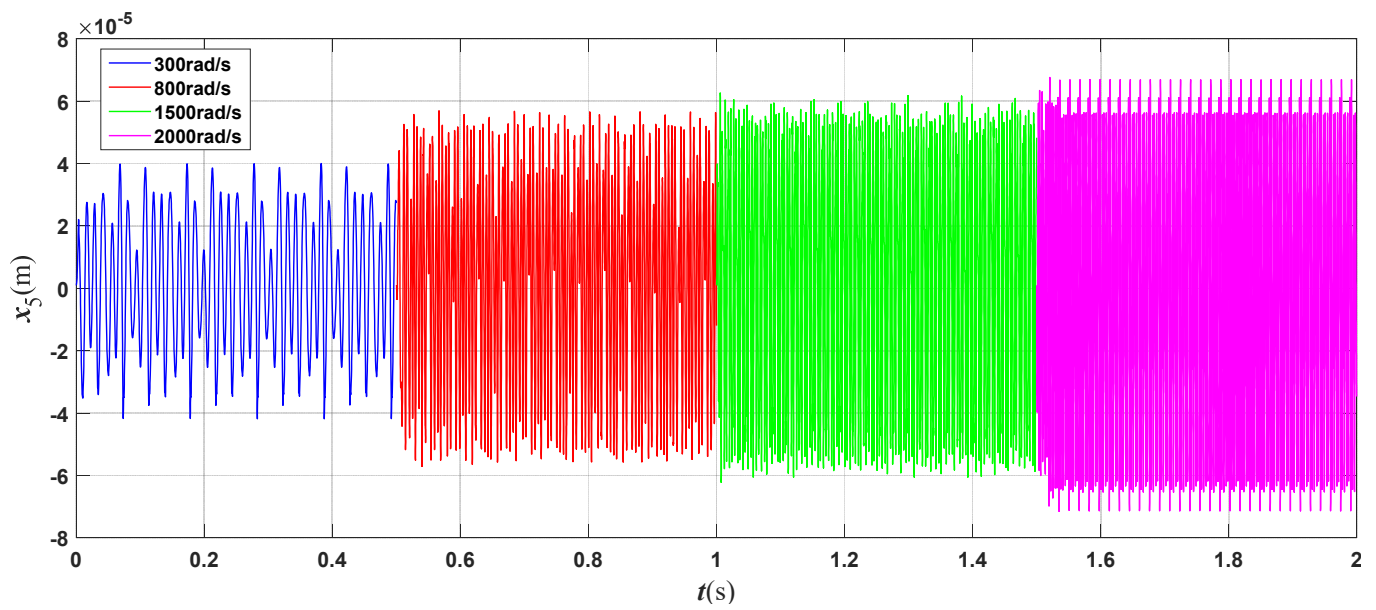


Figure 10. Time history diagram at each typical rotational speed.

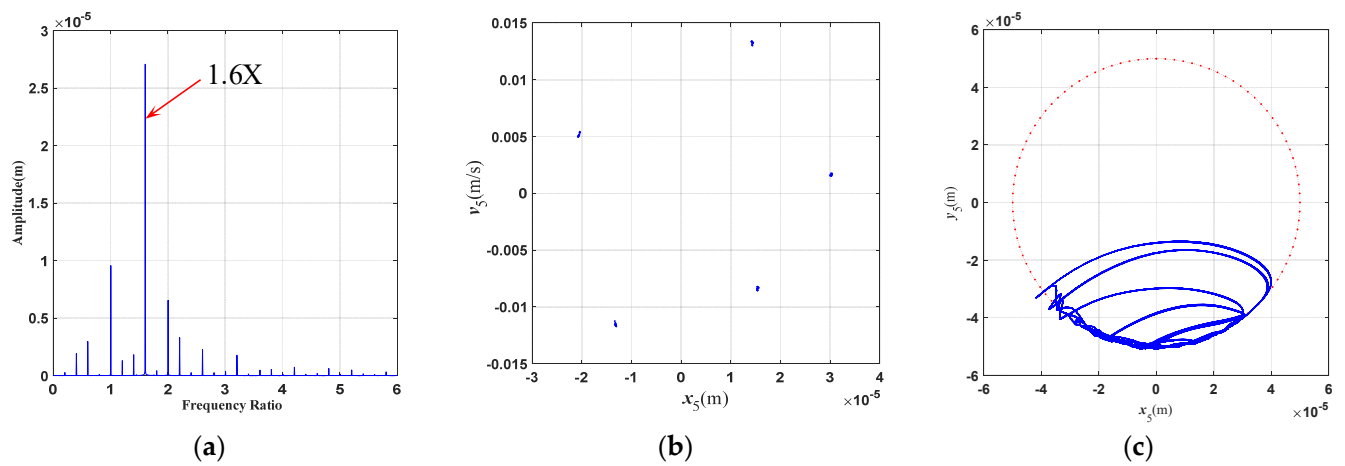


Figure 11. (a) Spectrum, (b) Poincaré maps, and (c) axis trajectory maps for  $\omega = 300$  rad/s.

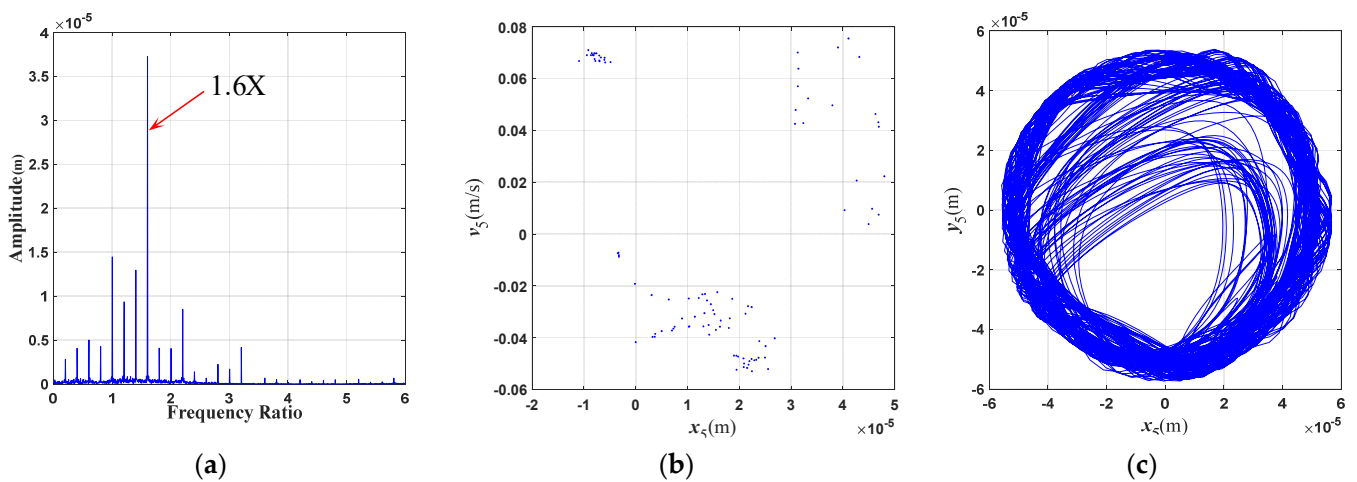


Figure 12. (a) Spectrum, (b) Poincaré maps, and (c) axis trajectory maps for  $\omega = 800$  rad/s.

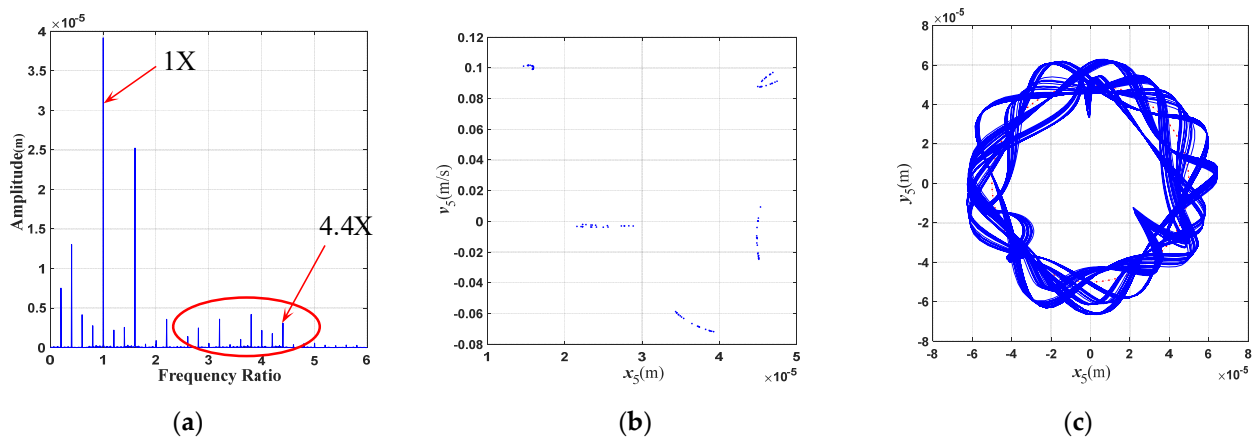


Figure 13. (a) Spectrum, (b) Poincaré maps, and (c) axis trajectory maps for  $\omega = 1500$  rad/s.

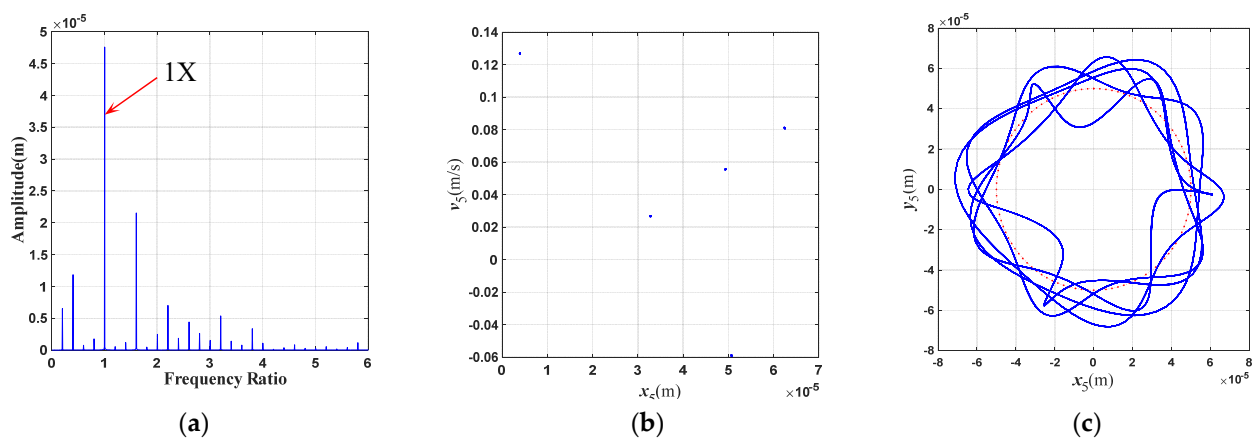


Figure 14. (a) Spectrum, (b) Poincaré maps, and (c) axis trajectory maps for  $\omega = 2000$  rad/s.

#### 4.2. Influence of Misalignment Parameters

Two shafts are connected by a clutch in the multi-rotor system. There will be misalignment at the clutch due to manufacturing and installation errors, and this misalignment has an important effect on the dynamic characteristics of the system. This misalignment mainly includes the parallel misalignment and the angle misalignment.

##### 4.2.1. Parallel Misalignment

The parallel misalignment is selected as the control variable to investigate the effect of parallel misalignment on the nonlinear response of the multi-rotor system, and the waterfall diagram of the vibration amplitude with the parallel misalignment and the frequency ratio is drawn, as shown in Figure 15. The relevant parameters are as follows: the rotational speed  $\omega_2 = 1500$  rad/s, the angle misalignment is 0, the frequency ratio is in the range of 0.1 to 0.6, and its step size is 0.01; the parallel misalignment is from 0 to  $1 \times 10^{-4}$  m, and its step size is  $3 \times 10^{-6}$  m, and the other parameters are consistent with Section 4.1. It can be seen in Figure 15 that with an increase in the parallel misalignment, the amplitude of the LP turbine decreases as a whole. It can be deduced that the parallel misalignment can inhibit the vibration of the LP turbine to some extent. The causes of this phenomenon are analyzed and are as follows. In the misalignment–rubbing coupling fault system, the additional bending moment caused by the parallel misalignment is linear, while the rubbing force caused by the rub-impact is nonlinear; when the parallel misalignment fault enhances gradually and becomes the dominant fault in the coupling faults, the vibrational response of system with the coupling faults is dominated by the misalignment vibration characteristics, and the chaotic and quasi-periodic motions caused by the nonlinear rubbing

force are inhibited. Therefore, the parallel misalignment can suppress the vibration of the low-pressure turbines to some extent.

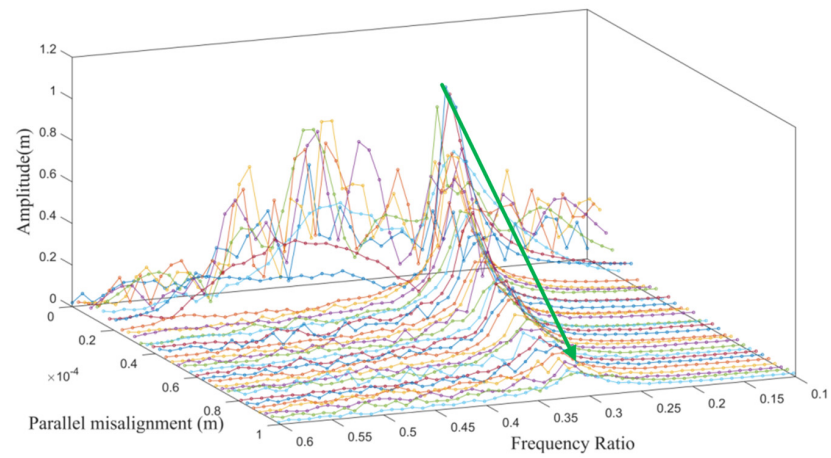


**Figure 15.** The waterfall diagram of the LP turbine with different parameters of parallel misalignment.

The parallel misalignment parameters  $\Delta e = 1 \times 10^{-5} \text{ m}$ ,  $3 \times 10^{-5} \text{ m}$ ,  $9 \times 10^{-5} \text{ m}$  are selected, respectively, for studying the typical nonlinear behaviors of the system; and the corresponding time history, the spectrum, and the Poincaré and axis trajectory maps are drawn, respectively, as shown in Figures 16–18. It can be shown from Figure 16 that, when the parallel misalignment  $\Delta e = 1 \times 10^{-5} \text{ m}$ , Figure 16c shows some points, and two of these points each pair up together; the orbit diagrams of the axle center of the LP turbine (Figure 16d) is a relatively clear and regular circle that is always beyond the red circle (the red circle is the boundary circle of whether rub-collision occurs), and it is inferred that the whole cycle’s rub-collision occurs between the rotor and the stator. When the parallel misalignment  $\Delta e = 3 \times 10^{-5} \text{ m}$ , Figure 17c shows five isolated points, denoting that the rotor is under the motion state of Period-5, and the axis trajectory is a more complex circle, as seen in Figure 17d. When the parallel misalignment  $\Delta e = 9 \times 10^{-5} \text{ mm}$ , Figure 18c shows five clusters of irregular scattered points, denoting that the rotor is in a quasi-periodic state. It can be seen in Figures 16b, 17b and 18b that, with the increase in the parallel misalignment, the relative relationship of each frequency component of the rotor system with misalignment and rub-collision coupling faults changes, and the amplitude of  $2\times$  gradually increases, which is positively correlated with the increase in the misalignment, and the amplitude of  $0.4\times$  is relatively decreased. It can be deduced that the parallel misalignment can inhibit rub-collision vibration to a certain extent, which is consistent with the conclusion of Figure 15.

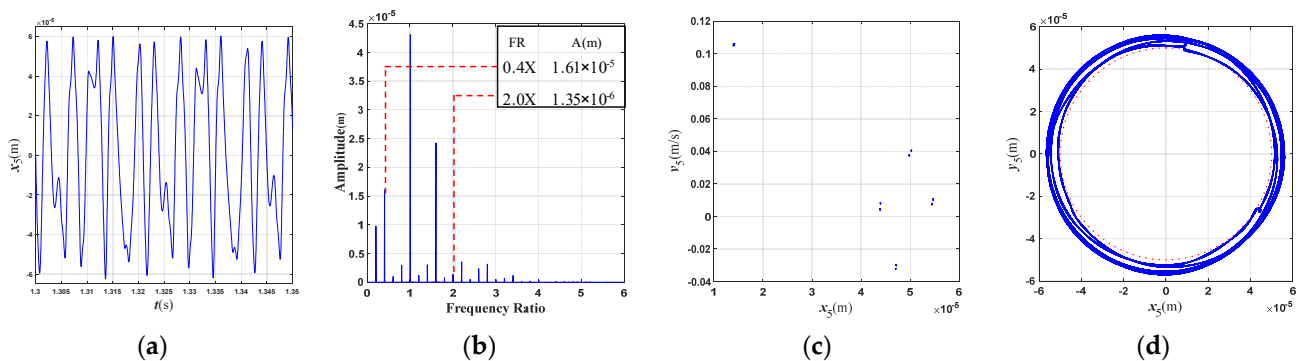


**Figure 16.** (a) Time history, (b) spectrum, (c) Poincaré maps, and (d) orbit diagram of shaft center for  $\Delta e = 1 \times 10^{-5}$ .

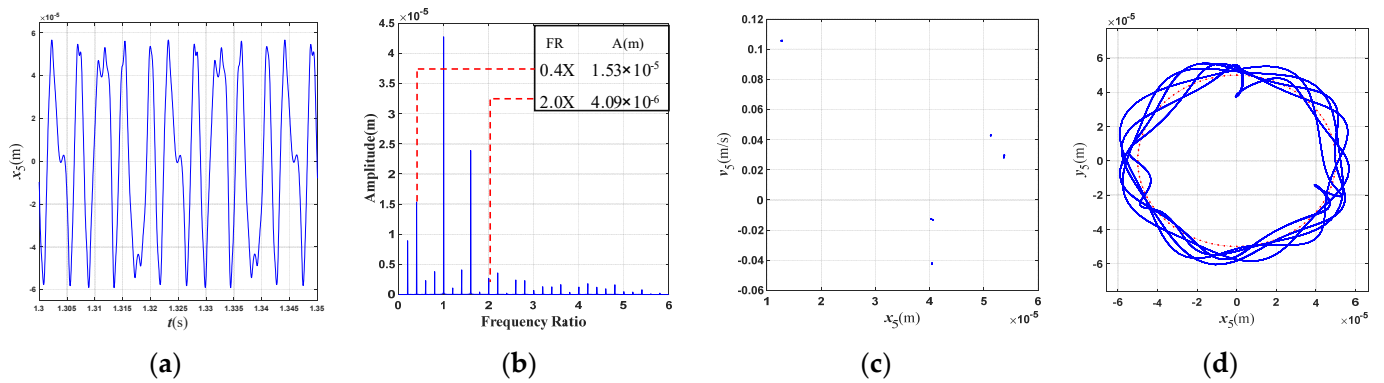


**Figure 17.** (a) Time history, (b) spectrum, (c) Poincaré maps, and (d) orbit diagram of shaft center for  $\Delta e = 3 \times 10^{-5}$ .

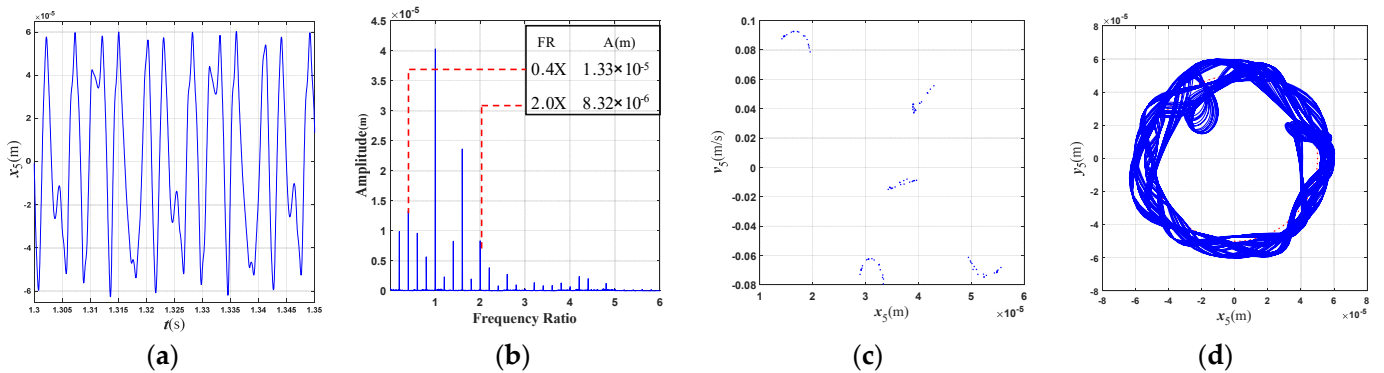


**Figure 18.** (a) Time history, (b) spectrum, (c) Poincaré maps, and (d) orbit diagram of shaft center for  $\Delta e = 9 \times 10^{-5}$ .

#### 4.2.2. Angle Misalignment

For studying the impact of angle misalignment on the dynamic response of multi-rotor system, the angle misalignment is selected as the control variable, and the waterfall diagram of vibration amplitude with angle misalignment and frequency ratio is drawn, as shown from Figure 19. The relevant parameters are as follows, the rotating speed  $\omega_2 = 1500$  rad/s, the parallel misalignment is 0, the frequency ratio is from 0.1 to 0.6, and its step size is 0.01; the angle misalignment is in the range of  $0^\circ$  to  $10^\circ$ , the step size is  $3 \times 10^{-6}$ , and the other parameters are consistent with Section 4.1. It can be seen in Figure 19 that, as the angle misalignment increases, the vibration amplitude of the LP turbine increases, which is more significant at low-frequency ratios.

In order to study the impact of this parameter on the typical nonlinear behaviors of the rotor, the misalignment angles  $\alpha = 2^\circ, 5^\circ, 8^\circ$  are selected, respectively, and the corresponding time history, spectrum, Poincaré and axis trajectory diagrams are drawn, as shown in Figures 20–22. It can be shown from Figure 20 that, when the misalignment angle  $\alpha = 2^\circ$ , the dominant frequency is  $1\times$ , and there is no obvious high-frequency doubling, as shown in Figure 20a. Figure 20c shows five isolated points, and Figure 20d presents some complex irregular circles, indicating that the rotor is in the motion state of Period-5. When the misalignment angle  $\alpha = 5^\circ$ , the amplitudes of  $1\times$  and  $0.4\times$  decrease, and some significant high frequency components such as  $2.2\times, 3.2\times, 3.8\times$ , and  $4.4\times$  appear, as seen in Figure 21b. Figure 21c shows five piles of irregular scattered points, denoting that the rotor is in a quasi-periodic state. When the misalignment angle  $\alpha = 8^\circ$ , the frequency history is extremely complex, the amplitudes of  $1\times$  and  $0.4\times$  continue to decrease, and the amplitude of  $3.2\times$  increases significantly, as shown in Figure 22b. The axis trajectory is extremely chaotic (Figure 22d), and Figure 22c shows a large number of irregular scatters, denoting that the system is in a chaotic state at this time. It can be seen in Figures 20a, 21a and 22a

that, as the angle misalignment increases, the vibration displacement of the rotor increases. It can be seen in Figures 20b, 21b and 22b that, with the increase in the angle misalignment, the maximum amplitude gradually decreases, and the amplitude of  $0.4\times$ , as the feature frequency of the rub-collision, also decreases. It can be inferred that the angle misalignment restrains the rub-collision vibration. The high frequency amplitude increases relatively, especially  $3.2\times$ . It is evident that the angle misalignment has an obvious influence on the vibration energy distribution. Compared with Section 4.2.1, the enlargement of the angle misalignment does not change the amplitudes of the misalignment feature frequency  $2\times$ , and it indicates that  $2\times$  is mainly excited by the parallel mismatch.

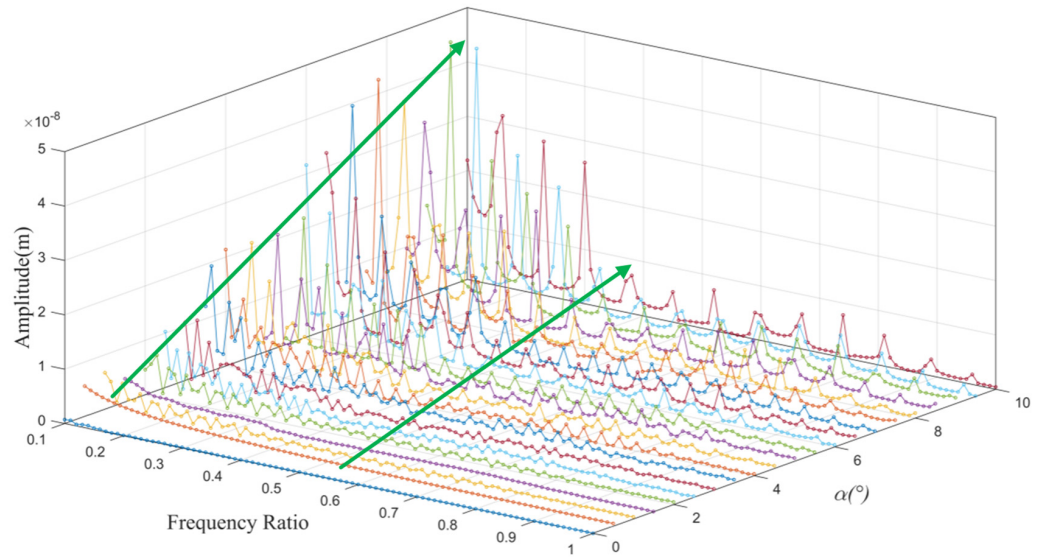


Figure 19. The waterfall diagram of LP turbine with change in angle misalignment.

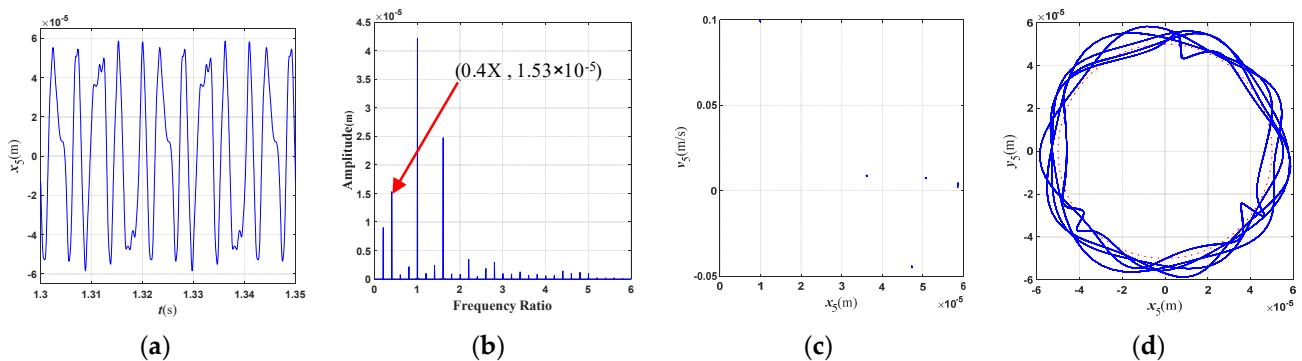


Figure 20. (a) Time history, (b) spectrum, (c) Poincaré maps, and (d) orbit diagram of shaft center for  $\alpha = 2^\circ$ .

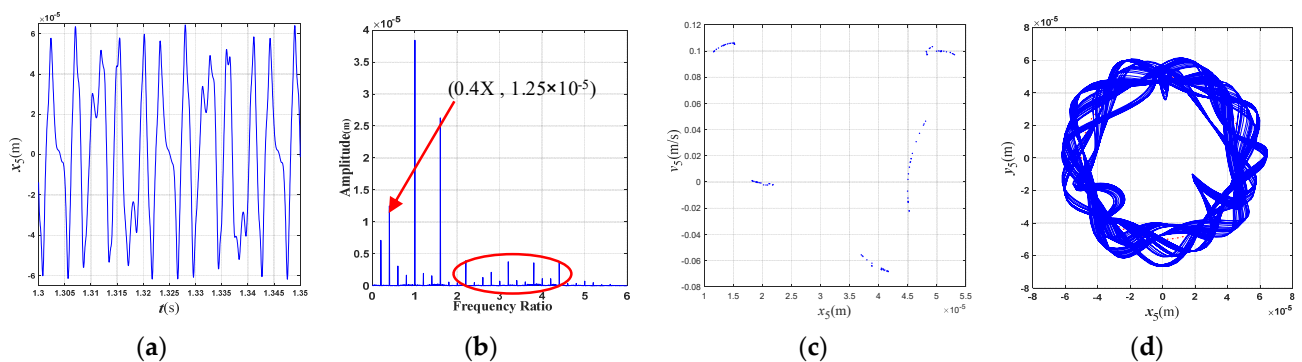
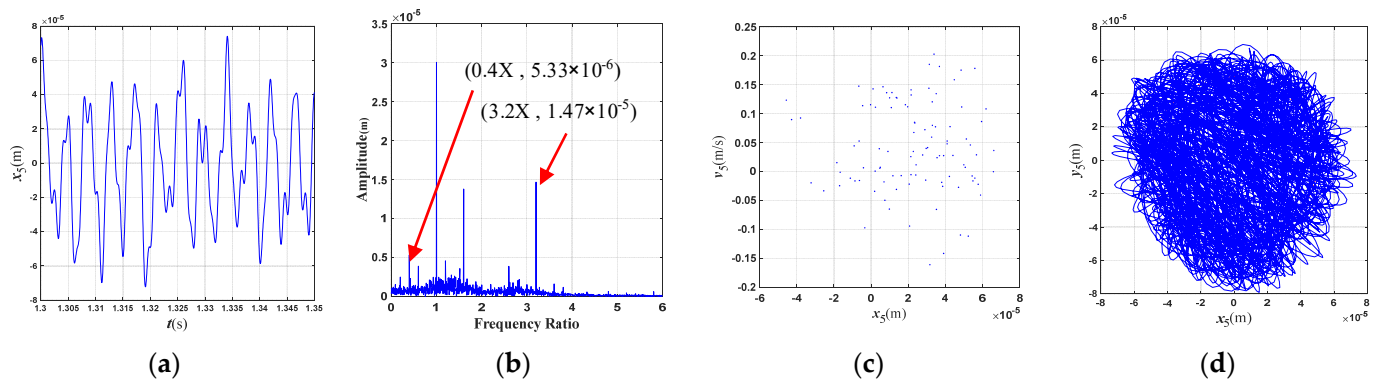


Figure 21. (a) Time history, (b) spectrum, (c) Poincaré maps, and (d) orbit diagram of shaft center for  $\alpha = 5^\circ$ .



**Figure 22.** (a) Time history, (b) spectrum, (c) Poincaré maps, and (d) orbit diagram of shaft center for  $\alpha = 8^\circ$ .

### 4.3. Influence of Rub-Collision Parameters

The rub-collision between the stator and the rotor occurs when the amplitude of the rotor vibration is greater than the static clearance. The multi-rotor system is subject to additional forces during the rub-collision transient state; thus, the dynamical behavior of the rotor changes. The impact of the rub-collision stiffness and friction coefficient on the nonlinear behaviors of the multi-rotor system is studied in this section.

#### 4.3.1. Rub-Collision Stiffness

For investigating the impact of rub-collision stiffness on the multi-rotor system with coupling faults, the rub-collision stiffnesses  $k_{p2} = 4 \times 10^7$  N/m and  $4 \times 10^9$  N/m are chosen, respectively, to calculate the time history, the spectrum, and the Poincaré and axis trajectory figures, as shown in Figures 23 and 24, and the rotating speed  $\omega_2$  is 1500 rad/s, and the other parameters remain unchanged. As can be shown in Figure 23a and the C zone of Figures 10 and 24a, when the rub-collision stiffness increases, the vibration displacement of the LP turbine decreases, and this is because the larger stiffness is more effective for the vibration reduction; it can be shown from Figures 13a, 23b and 24b that the amplitude of the characteristic frequency ( $0.4\times$ ) for rub-collision increases with the increase in the stiffness; Figure 23c shows the Period-5 motion, Figure 13 shows the quasi-periodic motion, and Figure 24 shows the chaotic motion state; it is deduced from Figures 13, 23 and 24 that the motion state of system changes significantly, and the nonlinear characteristic gradually increases with the increase in stiffness.

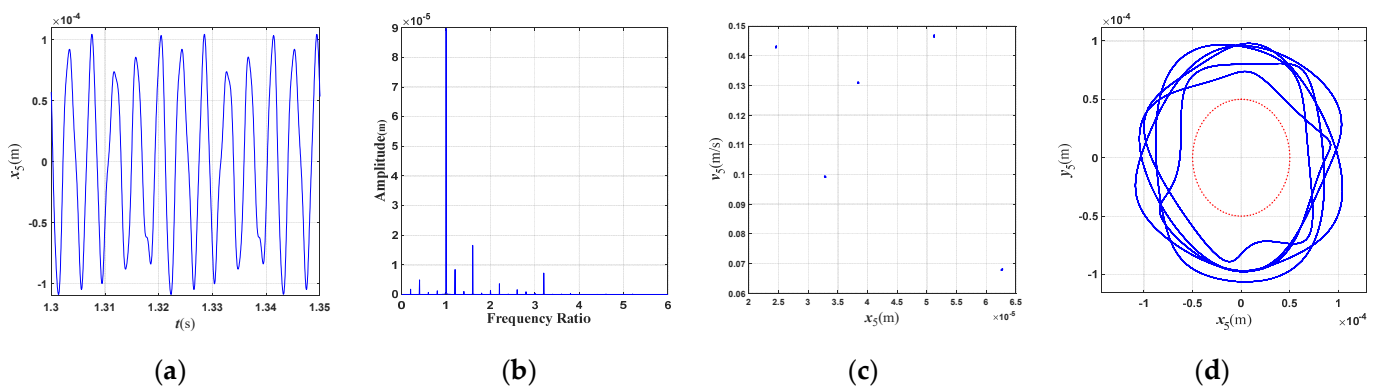


**Figure 23.** (a) Time history, (b) spectrum, (c) Poincaré maps, and (d) Orbit diagram of shaft center for  $k_{p2} = 4 \times 10^7$  N/m.

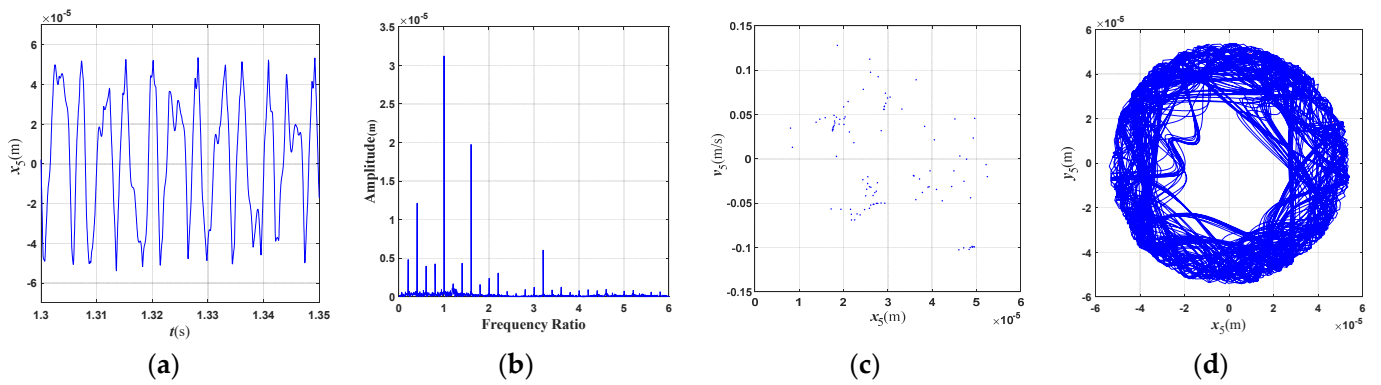


**Figure 24.** (a) Time history, (b) spectrum, (c) Poincaré maps, and (d) orbit diagram of shaft center for  $k_{p2} = 4 \times 10^9$  N/m.

### 4.3.2. Friction Coefficient

The coefficient of friction has a direct impact on the tangential rub-collision forces and then on the nonlinear behavior of the system. For researching the effect of the friction coefficient on the multi-rotor system with coupling faults, the friction coefficients  $f_2 = 0.02$  and  $0.2$  are chosen, respectively, to obtain the time history, the spectrum, and the Poincaré and axis trajectory figures, as shown in Figures 25 and 26, and the rotating speed  $\omega_2$  is  $1500$  rad/s, and the other parameters remain unchanged.

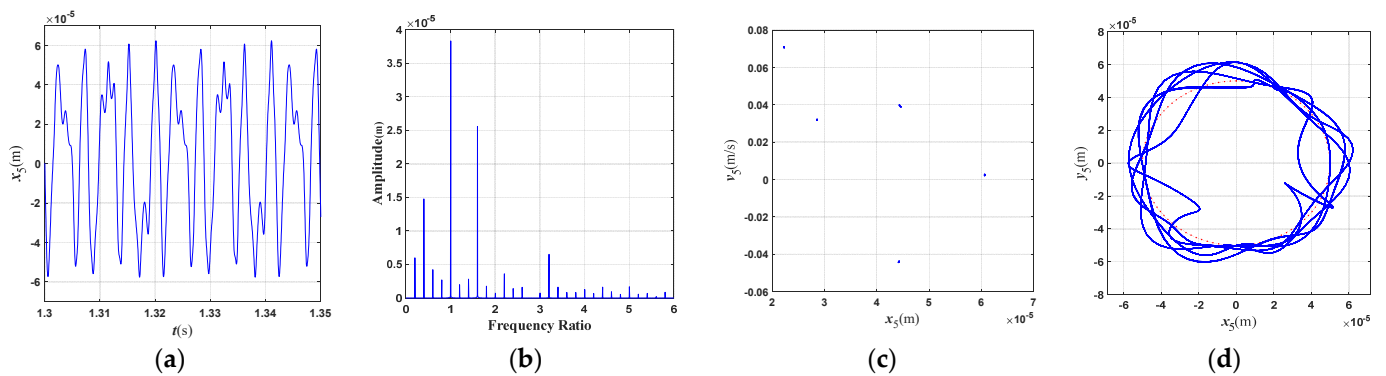


**Figure 25.** (a) Time history, (b) spectrum, (c) Poincaré maps, and (d) orbit diagram of shaft center for  $f_2 = 0.02$ .

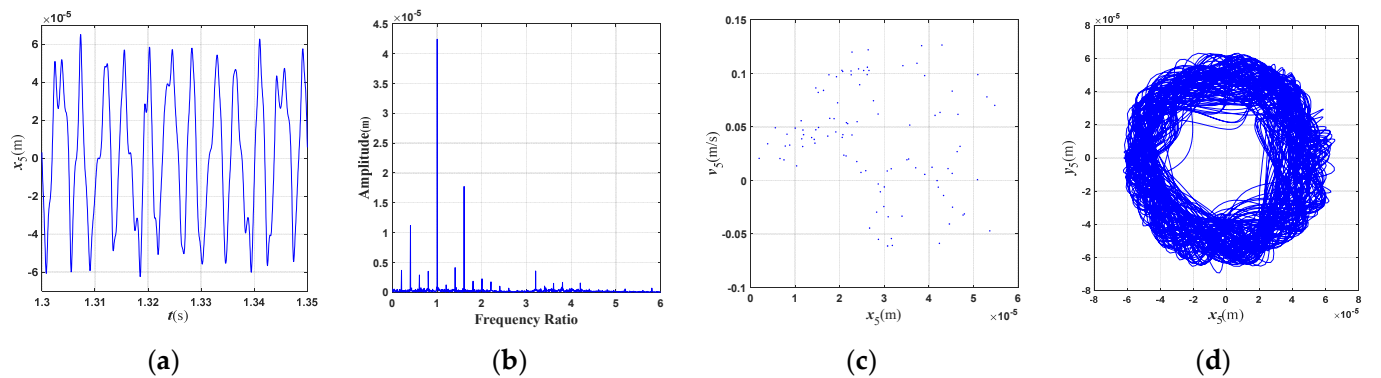


**Figure 26.** (a) Time history, (b) spectrum, (c) Poincaré maps, and (d) orbit diagram of shaft center for  $f_2 = 0.2$ .

It can be shown from Figure 25a and the C zone of Figures 10 and 26a that when the friction coefficient increases, the vibration displacement of the LP turbine remains essentially constant,

and this is because the increase in friction coefficient does not lead to the change in the rub-collision radial component  $P_n$ ; it can be shown from Figures 13a, 25b and 26b that the amplitude of the characteristic frequency ( $0.4\times$ ) for rub-collision decreases with the increase in the stiffness; Figure 25c shows the Period-5 motion, Figure 13 is the quasi-periodic motion, and Figure 26 shows the chaotic motion state; it is deduced from Figures 13, 25 and 26 that the motion state of system changes significantly, and the nonlinear characteristics strengthen with the increase in the friction coefficient.

#### 4.4. Influence of Wall Thickness

For improving the thrust–weight ratio of the aviation engine, the shaft is often designed as a hollow structure. For studying the effect of the wall thickness of the hollow shaft on the dynamical behaviors of the multi-rotor system, the wall thickness of the shaft for the LP compressor is selected as the control variable, and the outer diameter of the shaft and other parameters are consistent with Section 3.1. The waterfall diagrams of vibration displacement with speed and frequency ratio for the low-pressure compressor are drawn, as shown in Figures 27 and 28. Figure 27 is the waterfall diagram of vibrational response of low-pressure compressor under the different wall thickness values when the system has no fault. It can be shown from Figure 27 that, as the wall thickness of the shaft increases, the second-order peak speed increases, while the first-order peak speed is almost unchanged. Figure 28 is a waterfall diagram of the system with the coupling faults. As can be seen in Figure 28, the second-order peak speed increases with the increase in wall thickness, while the first-order peak speed remains unchanged, and these conclusions are consistent with those of the no-fault system. Comparing Figures 27 and 28, ( $0.4\times$  and  $2\times$ ) under the same wall thickness appear, as shown from the red circle of Figure 28, and these characteristics are consistent with the conclusion of the previous study.

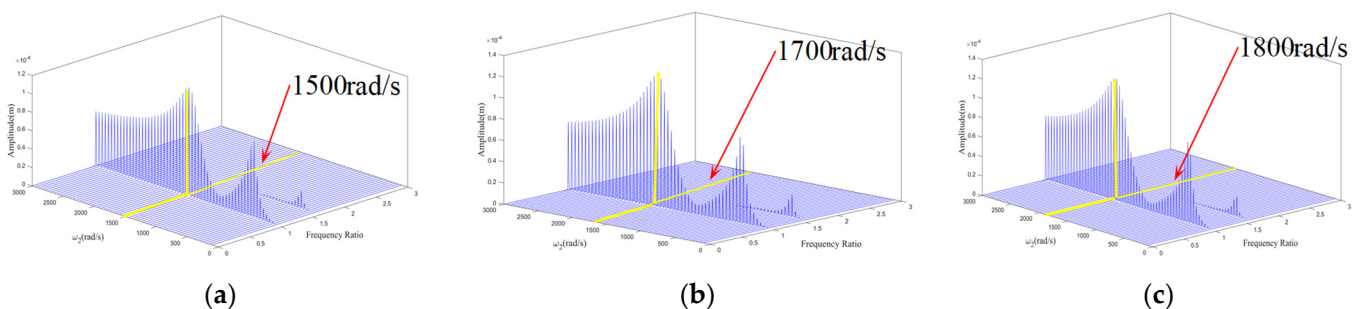


**Figure 27.** The waterfall diagrams of the fault-free LP compressor with different wall thicknesses: (a)  $\Delta d = 5$  mm; (b)  $\Delta d = 9$  mm; and (c)  $\Delta d = 15$  mm.

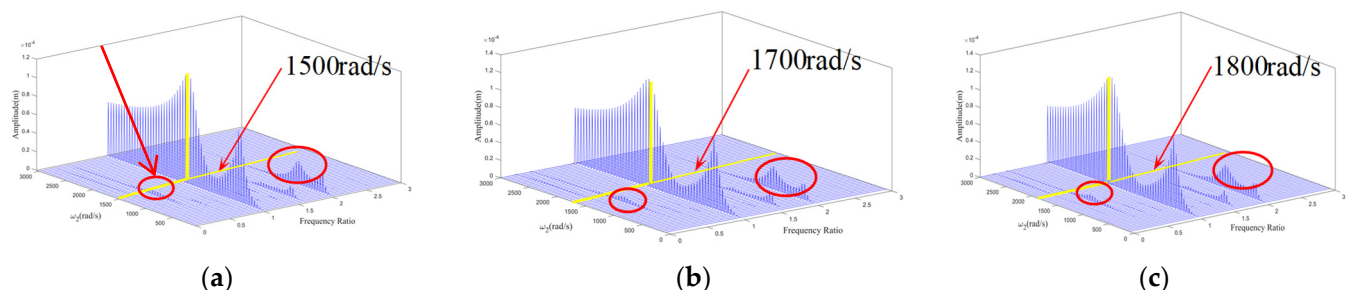


**Figure 28.** The waterfall diagrams of the LP compressor under coupling faults with different wall thicknesses: (a)  $\Delta d = 5$  mm; (b)  $\Delta d = 9$  mm; and (c)  $\Delta d = 15$  mm.

### 5. Validation of Theoretical Modeling Approach

There are some difficulties in the FE modeling of the misalignment and rub-impact coupling faults. The finite element analysis method is adopted to validate the correctness of

the theoretical model without fault. The validation of the model without fault can largely ensure the correctness of the subsequent fault model analysis. The specific steps are as follows: the geometric model of the rotor with a hollow shaft is established in the Geometry Module; then, it is imported as a transient structure; and the material property is defined according to the theoretical calculation. The bearings are equivalent to springs, one end of the spring is connected to the shaft, the other end is connected to the ground, and the stiffness of the springs is  $3 \times 10^6$  N/m. The rotor structure is meshed, the element size is 5 mm, the type of element is tetrahedral element Solid187, the number of elements is 141,640, the number of nodes is 219,146, and the finite element model is shown from Figure 29. The loads including the gravity, the unbalanced force, and the centrifugal force of the rotation speed of 1500 rad/s are applied to the rotor. The time history and frequency domain diagrams of the vibration displacement of the disc centroid are drawn. The results of the finite element method (FEM) and the results of the theoretical modeling approach (TMA) are compared, as shown in Figure 30a,b.

As the whole model parameter and constraints of the FE modeling are in accordance with the theory analysis, the results of the FEA and the TMA are comparable. It can be seen in Figure 30 that the theoretical calculation results are in good agreement with those of the finite element calculation, and this verifies the reliability of the TMA.



**Figure 29.** Finite element model and constraints of the LP turbine.

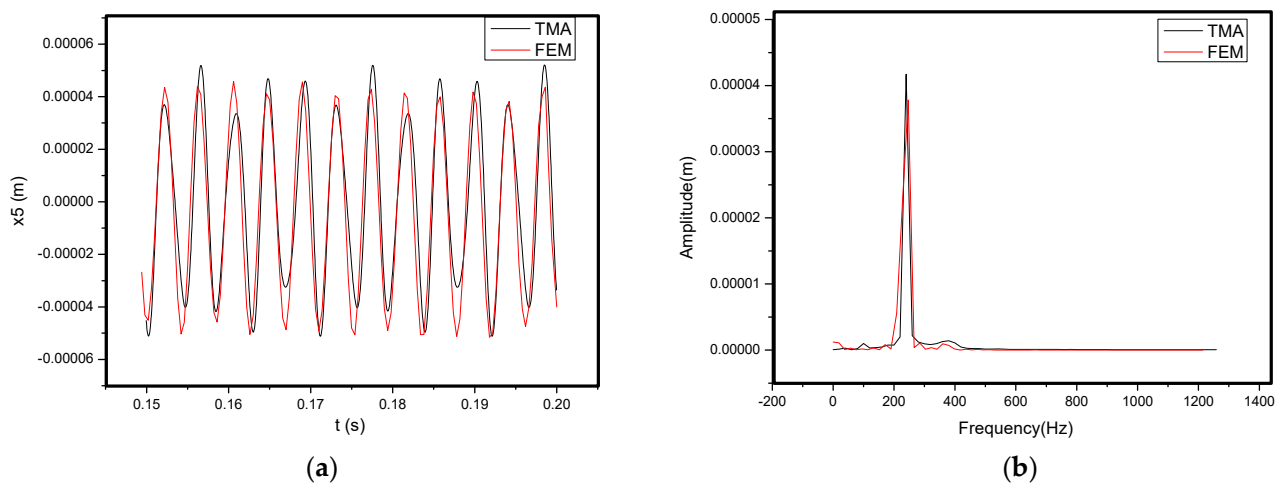


**Figure 30.** Comparison between FEM result and TMM result: (a) time history diagram and (b) frequency domain.

## 6. Conclusions

The dynamics of the three-rotor system with the coupling faults of rub-collision and misalignment is investigated by the theoretical modeling method, and the method is verified by the finite element analysis. The characteristic frequency of the fault for the multi-rotor system is analyzed, and the influence of the rotational speed, the rub-collision, the misalignment parameters, and the wall thickness of the hollow shaft on the dynamics is studied. The main research conclusions are as follows:

- (1) The characteristic frequency of the misalignment fault for this three-rotor system is  $2\times$ ; the characteristic frequency of the rub-collision fault is  $0.4\times$ , which is often accompanied by  $0.6\times$ ,  $2.2\times$ , and other frequency components. The characteristic frequency of coupling faults mainly includes  $2\times$ ,  $0.4\times$ ,  $0.6\times$ , etc., and the frequency component is more complicated than that of a single fault.
- (2) The rotating speed and clutch misalignment have essential influence on the nonlinear behaviors of the three-rotor system. The system exhibits complex dynamical behaviors such as periodic, multi-periodic, quasi-periodic, and chaos with an increase in the rotating speed. With the increase in the parallel misalignment, the amplitude of  $2\times$  gradually increases, and the amplitude of  $0.4\times$  is relatively decreased; the parallel misalignment can inhibit rub-collision vibration to a certain extent; as the angle misalignment enlarges, the vibration displacement of the rotor enlarges, and the amplitude of high frequency such as  $3.4\times$  increases relatively; the enlargement of the angle misalignment does not change the amplitude of the misalignment feature frequency, which is mainly excited by the parallel misalignment.
- (3) The motion state of the system changes significantly, and the nonlinear characteristics gradually strengthen with the enlargement of the rubbing parameters. When the rub-collision rigidity increases, the vibration displacement of the LP turbine decreases, the amplitude for the characteristic frequency ( $0.4\times$ ) of rub-collision increases, and the amplitude for the characteristic frequency of rub-collision decreases. When the friction coefficient increases, the vibration displacement of the LP turbine remains essentially constant. As the wall thickness of the shaft increases, the second critical rotating speed increases, while the first critical rotating speed is almost unchanged.

**Author Contributions:** Software (9.12.0.1884302 (MATLAB R2022a)), D.Y.; validation, H.W.; writing—original draft, G.N.; writing—review and editing, H.W. All authors have read and agreed to the published version of the manuscript.

**Funding:** This project is supported by National Natural Science Foundation of China (Grant No. 52275118).

**Data Availability Statement:** The raw data supporting the conclusions of this article will be made available by the authors on request.

**Conflicts of Interest:** The authors declare no conflicts of interest.

## References

1. Fu, C.; Zhu, W.; Zheng, Z.; Sun, C.; Yang, Y.; Lu, K. Nonlinear responses of a dual-rotor system with rub-collision fault subject to interval uncertain parameters. *Mech. Syst. Signal. Process.* **2022**, *170*, 108827. [[CrossRef](#)]
2. Pan, W.; Li, X.; Ling, L.; Qu, H. Dynamic modeling and response analysis of rub-collision rotor system with squeeze film damper under maneuvering load. *Appl. Math. Model.* **2023**, *114*, 544–582. [[CrossRef](#)]
3. Zhao, J.; Xing, L.; Ma, X.; Wang, Y.; Gao, D.; Du, G. Impact-Rubbings Dynamics Behavior of Magnetic-Liquid Double Suspension Bearing in Electromagnetic Failure Model. *Appl. Sci.* **2021**, *11*, 6345. [[CrossRef](#)]
4. Song, X.; Ren, Y.; Han, Q. Nonlinear vibration of rotating cylindrical shell due to unilateral contact induced tip rubbing impact: Theoretical and experimental verification. *Mech. Syst. Signal. Process.* **2022**, *164*, 108244. [[CrossRef](#)]
5. Zhang, X.; Yang, Y.; Ma, H.; Shi, M.; Wang, P. A novel diagnosis indicator for rub-collision of rotor system via energy method. *Mech. Syst. Signal. Process.* **2023**, *185*, 109825. [[CrossRef](#)]
6. Xu, M.; Zhang, H.; Miao, H.; Hao, J.; Li, C.; Song, W.; Yao, G.; Zhang, Y. Model-based vibration response analysis and experimental verification of lathe spindle-housing-belt system with rubbing. *Mech. Syst. Signal. Process.* **2023**, *186*, 109841. [[CrossRef](#)]
7. Hou, Y.; Cao, S.; Kang, Y. Study on the frequency modulation phenomenon in the rotor system with blade-casing rub-impact fault. *Int. J. Nonlin. Mech.* **2024**, *159*, 104626. [[CrossRef](#)]
8. Jin, Y.; Liu, Z.; Yang, Y.; Li, F.; Chen, Y. Nonlinear vibrations of a dual-rotor-bearing-coupling misalignment system with blade-casing rubbing. *J. Sound Vib.* **2021**, *497*, 115948. [[CrossRef](#)]
9. Li, Y.; Zhang, J.; Wang, L.; Chen, Y. A fault feature extraction method for rotor rubbing based on load identification and measured impact response. *Procedia Eng.* **2011**, *24*, 793–797.
10. Wang, N.; Jiang, D. Vibration response characteristics of a dual-rotor with unbalance-misalignment coupling faults: Theoretical analysis and experimental study. *Mech. Mach. Theory* **2018**, *125*, 207–219. [[CrossRef](#)]

11. Huang, W.; Tian, H.; Ma, H.; Wang, P.; Yang, Y.; Han, Q. An improved method for calculating the lateral and angular stiffness of spline couplings considering parallel misalignment. *Mech. Mach. Theory* **2023**, *189*, 105436. [[CrossRef](#)]
12. Tiwari, R.; Kumar, P. An innovative virtual trial misalignment approach for identification of unbalance, sensor and active magnetic bearing misalignment along with its stiffness parameters in a magnetically levitated flexible rotor system. *Mech. Syst. Signal. Process.* **2022**, *167*, 108540. [[CrossRef](#)]
13. Shinde, P.V.; Desavale, R.G. Application of dimension analysis and soft competitive tool to predict compound faults present in rotor-bearing systems. *Measurement* **2022**, *193*, 110984. [[CrossRef](#)]
14. Zhang, C.; Cao, P.; Zhu, R.; Chen, W.; Wang, D. Dynamic modeling and analysis of the spline joint-flexible coupling-rotor system with misalignment. *J. Sound Vib.* **2023**, *554*, 117696. [[CrossRef](#)]
15. Zhao, Y.; Wang, H.; Lin, J.; Han, Q.; Liu, Y. Effect of internal excitation induced by non-uniform contact of roller bearings on nonlinear vibration and stability of rotor system under combined loads. *Commun. Nonlinear Sci.* **2023**, *125*, 107381. [[CrossRef](#)]
16. Tang, H.; Ren, Y.; Xiang, J.; Kumar, A. Numerical and experimental analysis of rotor-bearing system for axial piston pump with misalignment–rubbing coupling fault. *J. Sound Vib.* **2023**, *559*, 117786. [[CrossRef](#)]
17. Xu, H.; Yang, Y.; Ma, H.; Luo, Z.; Li, X.; Han, Q.; Wen, B. Vibration characteristics of bearing-rotor systems with inner ring dynamic misalignment. *Int. J. Mech. Sci.* **2022**, *230*, 107536. [[CrossRef](#)]
18. Wang, P.; Yang, Y.; Ma, H.; Xu, H.; Li, X.; Luo, Z.; Wen, B. Vibration characteristics of rotor-bearing system with angular misalignment and cage fracture: Simulation and experiment. *Mech. Syst. Signal. Process.* **2023**, *182*, 109545. [[CrossRef](#)]
19. Wu, K.; Liu, Z.; Ding, Q.; Shackleton, P.; Cattley, R.; Gu, F.; Ball, A.D. Vibration responses of rotor systems in diesel multiple units under dynamic spatial misalignments and base motions. *J. Sound Vib.* **2021**, *492*, 115817. [[CrossRef](#)]
20. da Silva Tuckmantel, F.W.; Cavalca, K.L. Vibration signatures of a rotor-coupling-bearing system under angular misalignment. *Mech. Mach. Theory* **2019**, *133*, 559–583. [[CrossRef](#)]
21. Lees, A.W. Misalignment in rigidly coupled rotors. *J. Sound Vib.* **2007**, *305*, 261–271. [[CrossRef](#)]
22. Fu, X.Q.; Jia, W.T.; Xu, H.; Song, S.L. Imbalance–misalignment–rubbing coupling faults in hydraulic turbine vibration. *Optik* **2016**, *127*, 3708–3712. [[CrossRef](#)]
23. Lu, K.; Cheng, H.; Zhang, W.; Zhang, H.; Zhang, K.; Fu, C. Nonlinear dynamic behavior of a dual-rotor bearing system with coupling misalignment and rubbing faults. *Meas. Sci. Technol.* **2022**, *34*, 014005.
24. Jin, Y.; Hou, L.; Chen, Y.; Lu, Z. An effective crack position diagnosis method for the hollow shaft rotor system based on the convolutional neural network and deep metric learning. *Chin. J. Aeronaut.* **2022**, *35*, 242–254. [[CrossRef](#)]
25. Han, Z.; Wang, D.; Wang, Y.; Hong, J.; Cheng, R. Dynamic effects of the initial skewness of the inertial principal axis on the rotor with bolted joint. *Mech. Syst. Signal. Process.* **2023**, *200*, 110564. [[CrossRef](#)]
26. Chen, Y.; Hou, L.; Chen, G.; Song, H.; Lin, R.; Jin, Y.; Chen, Y. Nonlinear dynamics analysis of a dual-rotor-bearing-casing system based on a modified HB-AFT method. *Mech. Syst. Signal. Process.* **2023**, *185*, 109805. [[CrossRef](#)]
27. Fan, S.; Hong, L.; Jiang, J. Blue-Sky Catastrophic Bifurcations Behind Emergence and Disappearance of Quasiperiodic Rubbing Oscillations in a Piecewise Smooth Rotor–Stator System. *Int. J. Bifurcat. Chaos* **2022**, *32*, 2250221. [[CrossRef](#)]
28. Lu, K.; Jin, Y.; Huang, P.; Zhang, F.; Zhang, H.; Fu, C.; Chen, Y. The applications of POD method in dual rotor-bearing systems with coupling misalignment. *Mech. Syst. Signal. Process.* **2021**, *150*, 107236. [[CrossRef](#)]
29. Li, Q.; Zhang, W.; Chen, F.; Huang, G.; Wang, X.; Yuan, W.; Xiong, X. Fault diagnosis of nuclear power plant sliding bearing-rotor systems using deep convolutional generative adversarial networks. *Nucl. Eng. Technol.* **2024**. [[CrossRef](#)]
30. Xiang, L.; Zhang, X.; Zhang, Y.; Hu, A.; Bing, H. A novel method for rotor fault diagnosis based on deep transfer learning with simulated samples. *Measurement* **2023**, *207*, 112350. [[CrossRef](#)]

**Disclaimer/Publisher’s Note:** The statements, opinions and data contained in all publications are solely those of the individual author(s) and contributor(s) and not of MDPI and/or the editor(s). MDPI and/or the editor(s) disclaim responsibility for any injury to people or property resulting from any ideas, methods, instructions or products referred to in the content.